

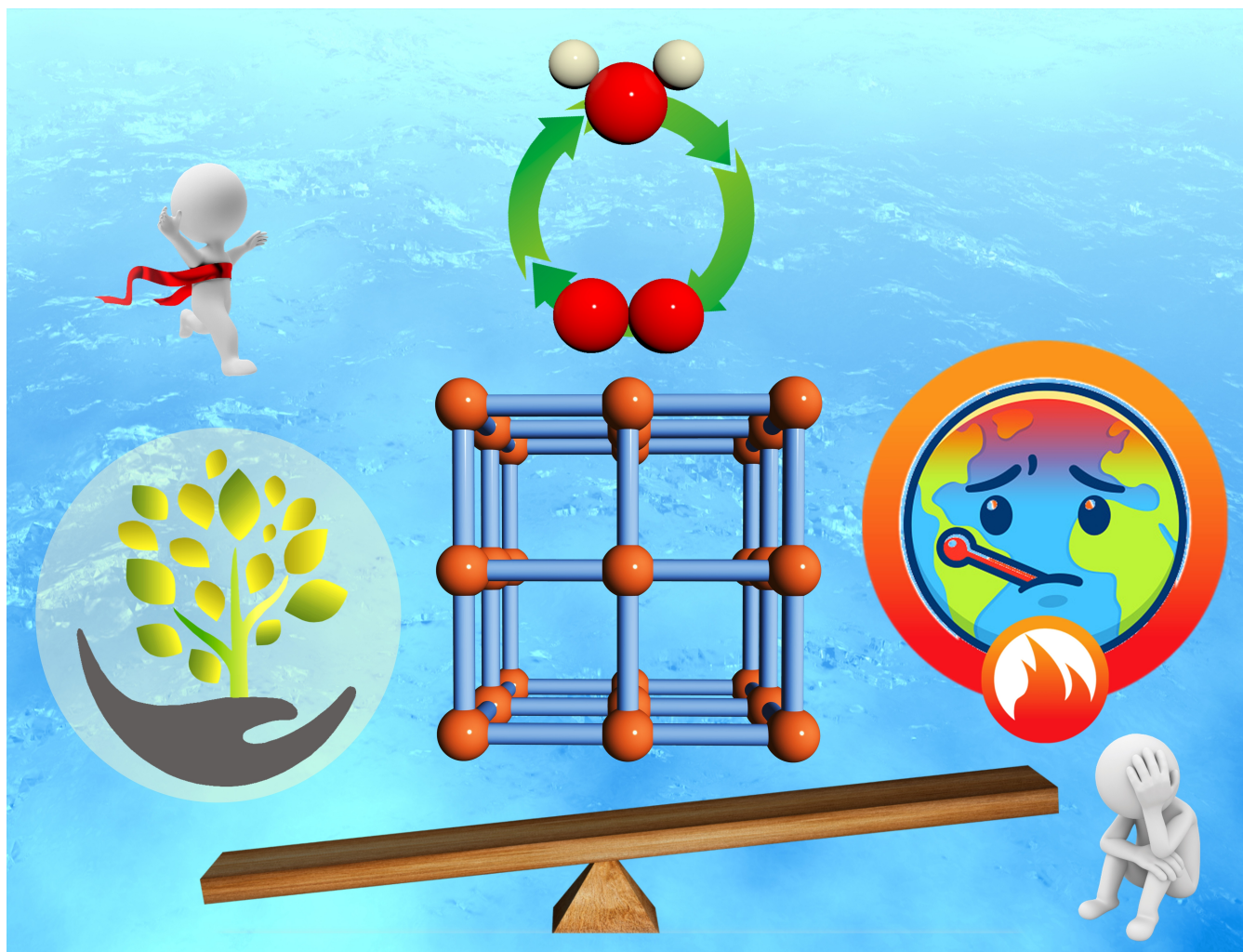
VIP Very Important Paper

Special
Collection

Avoiding Pyrolysis and Calcination: Advances in the Benign Routes Leading to MOF-Derived Electrocatalysts

Soumya Mukherjee,^[a] Shujin Hou,^[a, b] Sebastian A. Watzele,^[b] Batyr Garlyyev,^[b] Weijin Li,^{*[a]}
Aliaksandr S. Bandarenka,^{*[a, b]} and Roland A. Fischer^{*[a]}

Dedicated to Professor Wolfgang Schuhmann on the occasion of his 65th birthday



Taking cognizance of the United Nations Sustainable Development Goal 7 “affordable and clean energy”, metal–organic frameworks (MOFs) and derived materials have spurred research interest in electrocatalysis. New findings have made headway in water splitting (oxygen evolution reaction and hydrogen evolution reaction) and other electrocatalysis, including the oxygen reduction reaction and electrochemical CO₂ reduction.

Thanks to their structural versatility and compositional modularity, MOFs offer bespoke design paradigms for electrocatalyst development. Albeit most advances in this area are predicated upon direct carbonization (pyrolysis) of MOFs/MOF composites, eschewing these energy-intensive and high-cost methods, this review summarizes all recent advances in MOF-based electrocatalysts exclusively prepared through indirect post-treatments.

1. Introduction

Built from bottom-up self-assembly of metal ions or clusters linked by organic ligands, metal-organic frameworks (MOFs), a subclass of coordination networks, are (generally) crystalline framework solids featuring potential voids.^[1] Two decades of intensive research findings along this interface of molecular coordination chemistry and materials chemistry have catapulted MOFs into applications in storage/separations,^[2] catalysis,^[3] and sensing.^[4] Thanks to their structural periodicity and diversity that can be rationally fine-tuned, *i.e.*, the unique combination of compositional modularity, nanoporosity, and high surface areas,^[5] the high active site density and durability could be akin to state-of-the-art heterogeneous catalysts.^[6] In fact, the uniformly nanoporous channels in MOFs, in synergy with accessible active sites, have delivered record-high catalytic activities *versus* the traditional and/or typical heterogeneous catalysts. Thanks to their deference to the first principles of crystal engineering design,^[7] and reticular chemistry,^[8] adoption of MOFs can harmonize the dual benefits of both heterogeneous and homogeneous catalysts. Unsurprisingly, significant interests have spurred solid-state chemists to leverage MOFs for catalysis since the early days, which include chemical catalysis,^[6] photocatalysis,^[9] and electrocatalysis.^[10]

The ever-increasing energy crisis and environmental pollution have intensified the quest for renewable and green energy sources as viable alternatives to fossil fuels. H₂ is the most promising alternative, thanks to its high energy density and cheap, abundant source, *i.e.*, water.^[11] Water splitting, or water electrolysis is a straightforward process to produce H₂ [at the

cathode; H₂ evolution reaction (HER)], and O₂ [at the anode; O₂ evolution reaction (OER)], and this has great importance in terms of energy production (Scheme 1). The other environmentally benign energy conversion systems are H₂–O₂ fuel cells and metal-air batteries, whose reaction product is water.^[12] In this system, oxygen reduction reaction (ORR) is an inevitable cathode reaction (Scheme 1). Nevertheless, these green energy sources heavily rely upon electrocatalysts.

Electrocatalysis is at the forefront of several renewable energy storage and conversion technologies, offering sustainable routes to produce commodity chemicals and fuels.^[13] As aforementioned, electrochemical splitting of H₂O to enable H₂ and O₂ production are green routes perfectly aligned with the clean energy technologies of tomorrow. Targeting this pair, *viz.* HER and OER, finding inexpensive yet high-performing, stable electrocatalysts that refrain from the use of precious platinum group metals is the need of the hour. Likewise, the recent surge in fuel cells and metal-air battery research has fast-tracked advances in a) hydrogen oxidation reaction (HOR); b) ORR; c) N₂ reduction to evolve ammonia. Without utilizing platinum and/or other precious metals as aforementioned, delivering benchmark electrocatalytic performances from stable, robust electrocatalysts is an area of particular relevance, in direct alignment with the United Nations Sustainable Development Goal 7 “affordable and clean energy”.^[14]

1.1. Metal-organic frameworks for electrocatalysis

Embodying “nanomaterials by design”, the library of crystalline MOFs (> 100,000 and rising^[15]) leverage advantages from the principles of coordination chemistry, linking it with solid-state chemistry principles.^[16] Most MOF compositions comprise inexpensive first-row transition metals, Mn(II)/Mn(III), Fe(III), Co(II), Ni(II), Cu(II), Zn(II), *etc.* and low-cost, commercially available organic ligands (mostly carboxylates). This compositional aspect endows MOFs as promising earth-abundant electrocatalysts. Albeit a spur in research findings in the last ten years, major challenges are unmet, leaving several opportunities for utilizing MOFs as electrocatalysts. Consequently, question arises on the best routes of advancing MOF-based electrocatalysts (Figure 1).^[17]

One widely held paradigm is to use MOFs as precatalysts, *i.e.*, to afford 3D carbonaceous nanocomposites functionalized/embedded with transition metal species-based nanoparticles. The latter metallic component is exemplified by oxides, chalcogenides, oxypnictides, and pnictides. Regarding compositions of the metal-embedded carbonaceous composites, ligand

[a] Dr. S. Mukherjee, S. Hou, Dr. W. Li, Prof. Dr. A. S. Bandarenka, Prof. Dr. R. A. Fischer
Chair of Inorganic and Metal-Organic Chemistry
Catalysis Research Center, Ernst-Otto-Fischer Straße 1
and
Department of Chemistry
Technical University of Munich
Lichtenbergstraße 4, 85748 Garching b. München, Germany
E-mail: wj.li@tum.de
roland.fischer@tum.de

[b] S. Hou, S. A. Watzele, Dr. B. Garlyyev, Prof. Dr. A. S. Bandarenka
Physics of Energy Conversion and Storage, Physik-Department
Technical University of Munich
James-Franck-Str. 1, 85748 Garching b. München, Germany
E-mail: bandarenka@ph.tum.de

An invited contribution to the Wolfgang Schuhmann Festschrift

© 2021 The Authors. ChemElectroChem published by Wiley-VCH GmbH. This is an open access article under the terms of the Creative Commons Attribution Non-Commercial NoDerivs License, which permits use and distribution in any medium, provided the original work is properly cited, the use is non-commercial and no modifications or adaptations are made.

pyrolysis directly contributes to the carbon content, whereas metal ions/clusters give rise to the metallic content. Relying upon its propensity to produce a high density of active sites dispersed across porous conductive carbon matrices, the recent literature on MOF-pyrolyzed phases has witnessed record-high electrocatalytic performances.^[18] Nonetheless, such a boost in electrocatalytic efficiency largely stems from the high surface

area, while suffering from limited (to negligible) scopes of accumulation, particularly with respect to the ideal layout of piling up catalytic activities from individual metal catalyst components. Perhaps as the most significant drawback, pyrolysis impairs the foremost asset of MOFs, *i.e.*, their fine-tuned metal-ligand coordination environments, turning out moot for electrocatalysis. In essence, pyrolysis of exotic ligand-



Soumya Mukherjee received his PhD in Chemistry from the Indian Institute of Science Education and Research Pune in 2017. Followed by a 3 years' postdoctoral research experience at Bernal Institute, University of Limerick (Ireland), Soumya joined Technical University of Munich (Germany) in January 2020, as an Alexander von Humboldt postdoctoral researcher. An awarded member of the Royal Society of Chemistry (MRSC) and a recipient of the Marie Curie Individual Fellowship, Soumya is keen to develop energy-efficient porous materials that foster environmental sustainability.



Shujin Hou is now pursuing PhD in the Department of Physics at Technical University of Munich. He received his Bachelor's degree in Chemical Engineering and Technology at Tianjin Polytechnic University (2015). Afterward, he obtained his Master degree in Material Science and Optoelectronics at East China Normal University (2018). His current research interests focus on MOF-based electrocatalysts for green energy applications.



Sebastian A. Watzle received his M.Sc. degree in physics in 2016 from Technical University of Munich (Germany), where he worked on benchmarking catalysts for water splitting reactions in the group of Energy Conversion and Storage. During his doctorate at the same chair, he focused on the characterization of electrode material and the synthesis of active nanostructured catalysts for fuel cell applications under the supervision of A. S. Bandarenka. He received a fellowship from the Nano-systems Initiative Munich and the International Graduate School of Science and Engineering. After receiving his PhD degree in 2020, he continued working as a postdoctoral researcher.



Batyr Garlyyev received a M.Sc. degree from Georgia Institute of Technology (Atlanta, USA) in 2013 and a PhD degree from the same institute in 2016, where he worked on the synthesis of nanostructured materials with Prof. Dr. M.A. El-Sayed. Thereafter, he started his postdoctoral research in the group of Prof. Dr. A. S. Bandarenka at Technical University of Munich (Germany), and since October of 2020, he has been a group leader at the same chair. His research focuses on electrocatalysis for green energy conversion technologies. In the summer of 2016, Dr. Garlyyev was awarded TUM University Foundation Fellowship.



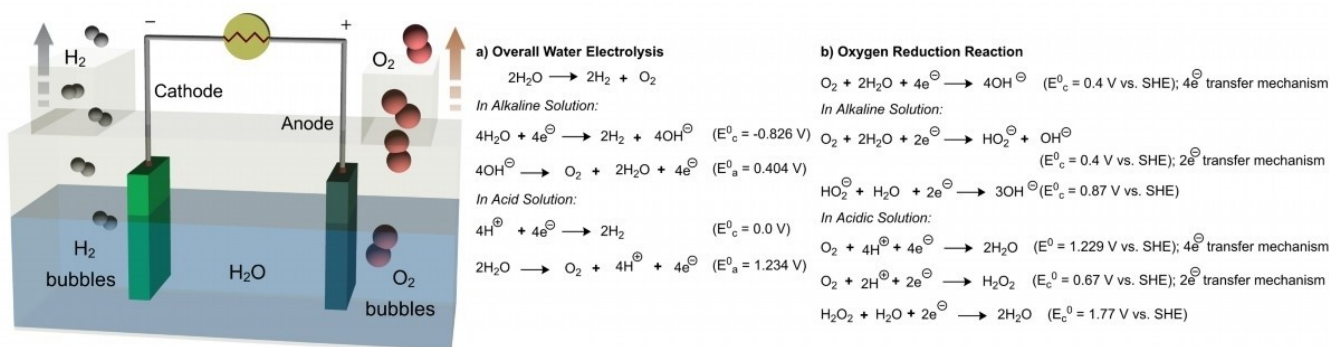
Weijin Li received his PhD in Fujian Institute of Research on the Structure of Matter, Chinese Academy of Sciences, in 2015. Followed a one-year postdoctoral research at the Collaborative Innovation Center of Chemistry for Energy Materials (2011-iChEM) of Xiamen University and five-year post-doc and subgroup leadership in Prof. Roland A. Fischer's group at Technical University of Munich under the support of Sino-Germany (CSC-DAAD) joint postdoctoral scholarship (2016-2017) and Humboldt Research Fellow (2017-2020), he is employed as a Junior Professor in the college of materials science and engineering, Nanjing University of Science and Technology with the research focusing on materials science for electromagnetism.



Aliaksandr S. Bandarenka received his PhD from Belarusian State University in 2005. After a post-doc at the University of Twente (Netherlands) and Technical University of Denmark, he joined the Center for Electrochemical Sciences (CES) at Ruhr University Bochum (Germany) as a group leader (2010-2014). Currently, he is an Associate Professor at the Department of Physics, Technical University of Munich (Germany). His research interests focus on developing electrocatalysts, methodologies for characterization and modification of electrified solid/liquid interfaces, and interfacial charge transfer.



Roland A. Fischer received his Dr. rer. nat. in 1989 and Habilitation in 1995 from Technical University Munich (TUM). He was Associate Professor at Heidelberg University (1996-1997) and Full Professor for Inorganic Chemistry at Ruhr-University Bochum (1997-2015). In 2016, he returned to TUM and took the Chair of Inorganic and Metal-Organic Chemistry. He was elected Vice President of the Deutsche Forschungsgemeinschaft in 2016. He is a member of the European Academy of Sciences. His research focuses on main group 13/transition metal compounds and clusters, precursors for metal-organic chemical vapor deposition and the materials chemistry of metal-organic frameworks.



Scheme 1. Schematic illustration of a) water splitting in an electrochemical cell, including b) ORR.

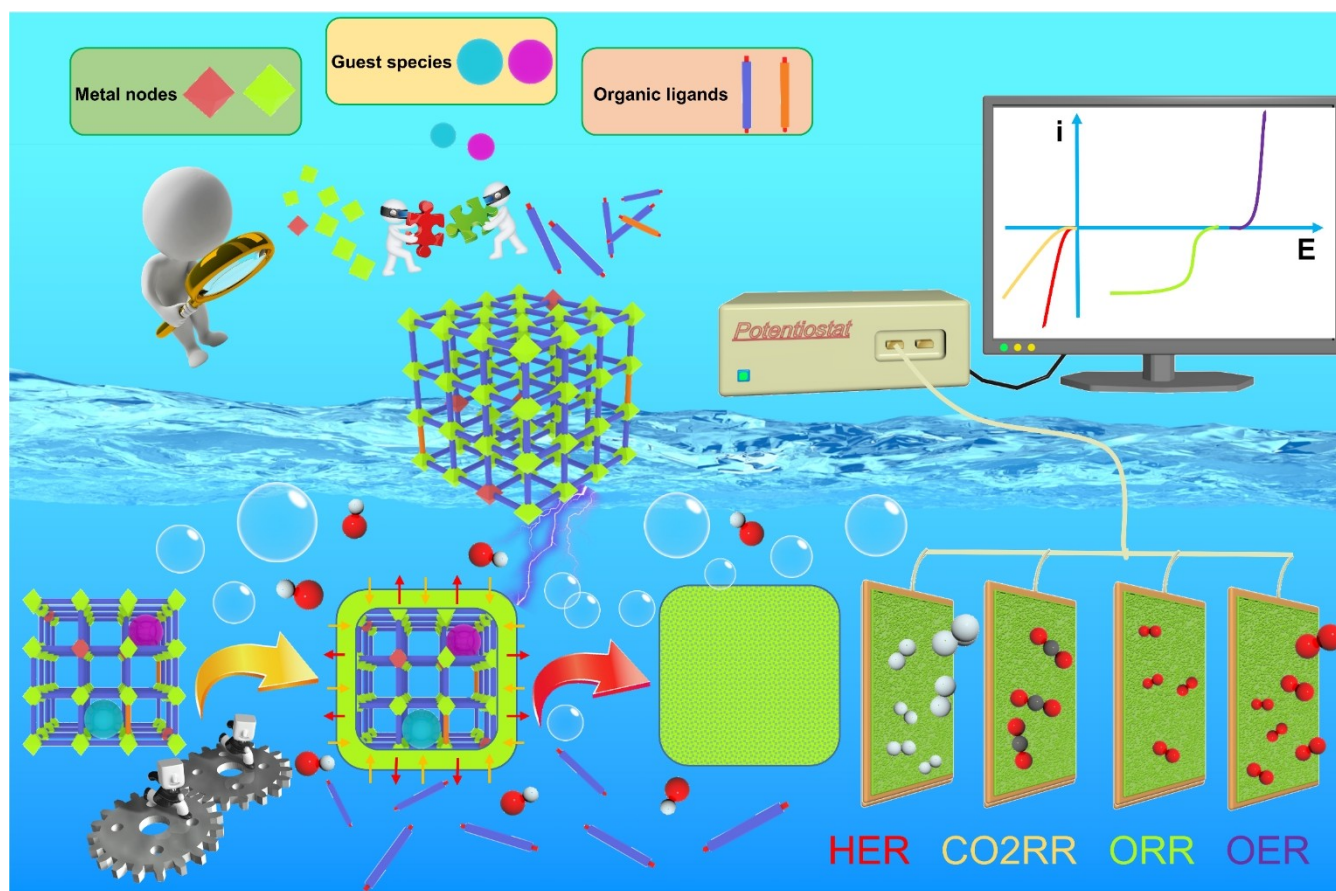


Figure 1. Schematic illustration of electrocatalytically active MOF derivatives prepared through indirect post-treatment routes, avoiding calcination or pyrolysis.

functionalized, high-cost MOFs to prepare nanocomposites, despite benchmark performances, suffers from a weak spot: the bottom-up MOF design approaches only contribute little to the electrocatalytic efficiencies. Then again, MOFs as the precursors to prepare single-atom catalysts (SACs) embedded in carbon nanostructures have emerged as an alternative route to success, albeit wrecking the framework architectures.^[18] On the flip side, direct use of MOFs can overcome most (or all) of the limitations mentioned above, but suffers from limited electrical conductivity and lack of optimal stability because of harsh conditions in

the purview of electrochemical reactions.^[6] Two factors dominate here: a) most organic ligands are redox-inactive; b) electronic interactions between the metal centers and organic ligands are weaker than those found in traditional solid-state materials, such as metallic oxides. This is why most MOFs demonstrate insulating nature, presenting a see-saw situation.^[19] Breaking this trade-off, thanks to a number of recent reports by us and others, conducting or semiconducting MOFs have recently come to the fore.^[20] The oft-encountered *catch-22* situations can be addressed by ultrathin MOFs.^[21]

Despite the rarity, thin nature minimizes the electrical transport distance, integrating well with the rationally selected conducting scaffolds to deliver high conductivity. In principle, the resulting *prêt-à-porter* MOF derivatives tend to be replete with a high unsaturated metal density, each catalytically active and therefore contributing to the catalytic performance.^[21]

In MOFs, metal ions and/or clusters are coordinated to organic ligands. Whereas electrocatalytic conditions (when extreme) can dissociate these coordination bonds, free metal ions or clusters can form, their assembled forms potentially acting as catalysts. Kinetics of this disassembly-reassembly transition gets influenced by the metal-ligand bond strength, delivering electronic and crystal structures amenable for highly active sites. As a result, structural features of the re-constructed MOF derivatives play dominant roles in dictating the catalytic efficiencies. In addition, metal types and their distribution in MOFs also impact the efficiencies significantly.^[22] This leads us to believe that investigating structural derivatization and the metal-ligand scaffold roles can unlock the design of highly efficient electrocatalysts in future. Unsurprisingly, these advantages have spawned several research findings of late. Several active-site rich MOF derivatives demonstrate HER, OER, ORR, and electrochemical CO₂ reduction reactions, as we review herein.^[21,23]

2. MOF Stability for Electrocatalysis

Electrocatalyst performance relies upon several key parameters. These primarily comprise onset potential, overpotential, Tafel slope, exchange current density, turnover frequency, Faradic efficiency, product selectivity and/or catalyst durability *vis-à-vis* stability.^[17a] Whereas MOF-carbonized or MOF-pyrolyzed carbon matrices tend to uphold electrocatalytic performances under the relevant 'harsh' conditions, moving away from these treatments and adopting indirect post-treatments imply that intrinsic metal-ligand bonds in the MOFs would be subjected to harsh reaction conditions. This is in particular reference to the MOFs' prolonged water stability, inertness to acidic and/or alkaline pH, and often poses a bottleneck in MOFs. MOFs' and MOF-derived hybrids' instability in the presence of water or harsh chemicals is largely because these are comprised of typically labile metal-organic bonds and sometimes accompanied by coordinatively unsaturated and reactive metal centers.^[24] Performance is compromised by generally poor selectivity.^[24b]

Whereas metal complex-based molecular OER catalysts get decomposed under OER conditions to afford metal oxide/hydroxide catalysts, the more reducing HER conditions retain the molecular metal complexes as catalysts.^[25] On the contrary, organic linkers in MOFs could be oxidized under OER conditions, leading to framework collapse. Simply put, MOFs, in such cases, will merely assume the role of precursors, *i.e.*, the "precatalysts", eventually generating the true OER catalysts.^[13] Consequently, to leverage MOFs in OER catalysis,^[26] or other oxidations,^[27] surface-sensitive structural characterizations should lead the way.^[28] In general, these techniques involve

Raman spectroscopy, X-ray photoelectron spectroscopy (XPS), and X-ray synchrotron spectroscopy, either monitoring before and after the reactions (*Ex-situ*), or during the reaction (*In-situ* and/or *In-operando*). Results typically reveal: a) whether the MOFs are indeed stable under the oxidative environments of OER; b) accurately determine the active catalysts on the surfaces. Meeting these stability criteria qualify some MOF derivatives as OER electrocatalysts, while a few select analogues turn out precatalysts, *i.e.*, precursors to metal oxide/hydroxide catalysts.^[25] Considering the lower overpotentials and milder conditions involved with electro-reduction, such as CO₂ reduction reaction (CO₂RR) and ORR, the stability of MOFs to these reaction conditions would be higher *versus* OER.

The majority of MOFs are sensitive to water exposure, either to liquid water or humidity. That water molecules are in opulence under water splitting conditions, and other electrocatalytic conditions such as CO₂RR imply the high relevance of MOF stability to aqueous electrolytes.^[29] Metal-ligand bond strength arguably contributes the most, largely dominated by Lewis acidity of the coordinated metal sites and the linkers' pK_a values.^[30] Water stability can be typically predicted from the principle of hard and soft acids and bases,^[31] where either a hard Lewis acid-hard Lewis base tie-up (*e.g.*, UiO-66,^[32] MIL-125(Ti)^[33]) or a soft Lewis acid-soft Lewis base pairing (*e.g.*, Ni₃(BTP)₂,^[34] Co(bdp)^[35]) culminates in high hydrolytic stability of the metal-ligand bonds. Lability of the metal cluster also contributes, leaving Group 4 metal cluster (Zr(IV), Ti(IV), Hf(IV)) based 'robust' MOF platforms at the upper echelon of stable MOFs (regardless of their insulating nature impeding electrocatalysis thus far).^[36]

3. MOF Derivatives for Electrocatalysis

3.1. OER and HER case studies: mechanisms manifested

3.1.1. MOF derivatives for OER: representative examples

3.1.1.1. Mechanism of OER

Due to its sluggish kinetics and multi-electron transfer, the half-reaction of water splitting, OER, is the limiting step in water electrolyzers.^[11,37] To understand the pivotal factors governing the activity of OER electrocatalysts, several mechanisms have been proposed according to the intermediates identified at the electrolyte-catalyst interface during the reaction. For instance, the conventional adsorbate evolution mechanism (AEM) is implemented on a tandem four concerted proton-electron transfer (CPET) mechanism occurring at the catalytically active metal sites (denoted as M) (described in Figure 2a). As regards OER, the proposed AEM steps in acidic and alkaline media are listed in Table 1.^[23a,37-38]

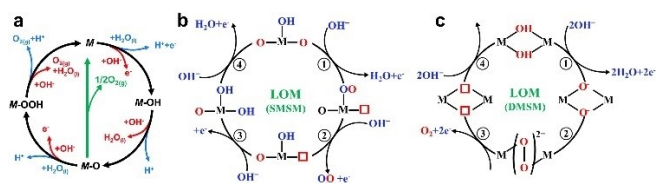


Figure 2. a) The adsorbate evolution mechanism (AEM) of OER in both acidic (blue line) and alkaline (red line) media. Reproduced with permission from Ref. [11]. Copyright 2017, Royal Society of Chemistry. b and c) The lattice oxygen oxidation mechanism (LOM) of OER in alkaline media, including the single-metal-site mechanism (SMSM) and dual-metal-site mechanism (DMSM). Red squares represent oxygen vacancy.

Table 1. Mechanism of OER, in acidic and alkaline media.

Acidic media
$M + H_2O \rightarrow M-OH + H^+ + e^-$ (1)
$M-OH \rightarrow M-O + H^+ + e^-$ (2)
$2 M-O \rightarrow O_2 + 2 M^+ + 2e^-$ or $M-O + H_2O \rightarrow M-OOH + H^+ + e^-$ (3)
$M-OOH \rightarrow M + O_2 + H^+ + e^-$ (4)
Alkaline media
$M + OH^- \rightarrow M-OH + e^-$ (5)
$M-OH + OH^- \rightarrow M-O + H_2O + e^-$ (6)
$2 M-O \rightarrow O_2 + 2 M^+ + 2e^-$ or $M-O + OH^- \rightarrow M-OOH + e^-$ (7)
$M-OOH + OH^- \rightarrow M + O_2 + H_2O + e^-$ (8)

3.1.1.2. OER active MOFs

In light of the dynamic structural variations observed at the OER catalyst surfaces, lattice oxygen oxidation mechanism or lattice oxygen-mediated mechanism (LOM) can enable OER. This arguably has a direct bearing on the ever-growing attempts to develop perovskite-type electrocatalysts.^[39] The activated lattice oxygen assumed around the active metal sites can directly couple with the deprotonated *O intermediate to form *OO species (*i.e.*, the single-metal-site mechanism (SMSM) in Figure 2b), and the latter is further converted into O₂ over the subsequent step. The oxygen vacancy caused by the consumed lattice oxygen can be subsequently refilled by OH⁻.^[40] According to the number of participated lattice oxygen, a dual-metal-site mechanism (DMSM) has also been proposed, as shown in Figure 2c. The adjacent activated lattice oxygen atoms facilitate the construction of M–OO–M intermediate, where O₂ is directly evolved, and two oxygen vacancies are generated.^[41] The recent flourish in experimental techniques, such as ¹⁸O isotope labeling,^[42] and O-based X-ray spectroscopy,^[43] have accelerated the all-inclusive comprehension on the LOM pathway and are expected to break the inherent limitations of scaling relationships between the *OH and *OOH intermediates in AEM. This is primarily because the rate-determining steps of *OH deprotonation and *OOH formation do not exist along the LOM catalytic cycle.^[44] Accordingly, LOM is considered one of the most promising mechanisms to guide OER activity improvement. Over the past few decades, substantial research efforts have gone into investing LOM on the state-of-the-art OER electrocatalysts, RuO₂,^[45] IrO₂,^[46] Zn-substituted CoO₂ slab,^[47] NiCo₂O₄,^[48] etc.

The development of previously unreported electrocatalyst types with high activity is another effective way of overcoming the constraints posed by slow water oxidation kinetics.^[49] Over the past few years, extensive studies have revealed a number of high-performing MOF-derived OER catalysts.^[23c,50] However, as far as MOF design rationales are concerned, systematic research-based targeted blueprints largely remain obscure. Particularly, preparing MOF-derived state-of-the-art catalysts under energy-efficient, mild conditions needs in-depth exploration. The following section outlines several advanced strategies on MOF-derived OER catalysts' preparation, including alkaline hydrolysis, electrochemical conversion, ion etching, and sulfuration.

MOF-based electrocatalysts have been widely studied for water oxidation owing to their well-defined metal sites, tunable compositions, and structures.^[2,26] However, the structure-performance relationships and origins of their superior OER activities remain elusive. Taking account of the MOF's hydrolytic stability in extremely acidic or alkaline electrolytes, more studies focus on the pre-catalytic chemical processing of the pristine MOFs.^[51] Especially, carboxylate-based MOFs are relatively fragile under strongly alkaline conditions (that OER entails), while OH⁻ ions can cleave the coordination bonds holding the carboxylate linkers to the metal sites, resulting in the formation of metal hydroxides.^[51b,52] Accordingly, some latest works have reported an alkaline hydrolysis strategy for delivering MOF-derived OER electrocatalysts.^[51a,53] As an example, Li and co-workers developed a facile alkali-etched method to obtain the defect-rich ultrathin Ni-MOF nanosheet array (D–Ni–MOF NSA) for OER.^[54] In alkaline electrolyte, partial coordinated Ni–O bonds of 2D MOFs could be broken due to KOH invasion, producing open unsaturated Ni(II) sites (Figure 3a).^[55] XRD patterns demonstrate clear retention of the Ni-MOF NSA diffractogram post-alkali etching treatment, evident of framework stability. The exposed (002) plane referring to the metal-oxide layers, however, shows a faint negative shift (Figure 3b). This result indicated an increased space between the metal-oxide layers after alkali etching treatment. Two reasons can likely cause such observation: a) breaking of the partially coordinated Ni–O bonds; b) the weakening of interactions between the neighboring layers. Meanwhile, a positive shift to the O 1s XPS spectra in D–Ni–MOF NSA can be found as compared to that in Ni-MOF NSA (Figures 3, c, and d). Notably, a peak at 530.9 eV shows a high XPS area ratio after alkali etching, indicating a high number of oxygen vacancies. This could be due to the breaking of Ni–O bonds after KOH intrusion. According to the Fourier-transformed k³χ(k) EXAFS spectra (Figure 3e), Ni-MOF and D–Ni–MOF display the same dominant peak at 1.60 Å, suggesting a coordinated nature of the Ni–O bonds. However, the low average coordination number in D–Ni–MOF further manifests the rich unsaturated Ni sites.

To improve the OER performance of MOF-derived electrocatalysts and to elucidate their structural conversion mechanisms, more studies have started to pay close attention to the completely reconstructed MOFs following alkaline hydrolysis.^[53,58] Using a mixed Fe–MOFs@Ni–MOFs hybrid plat-

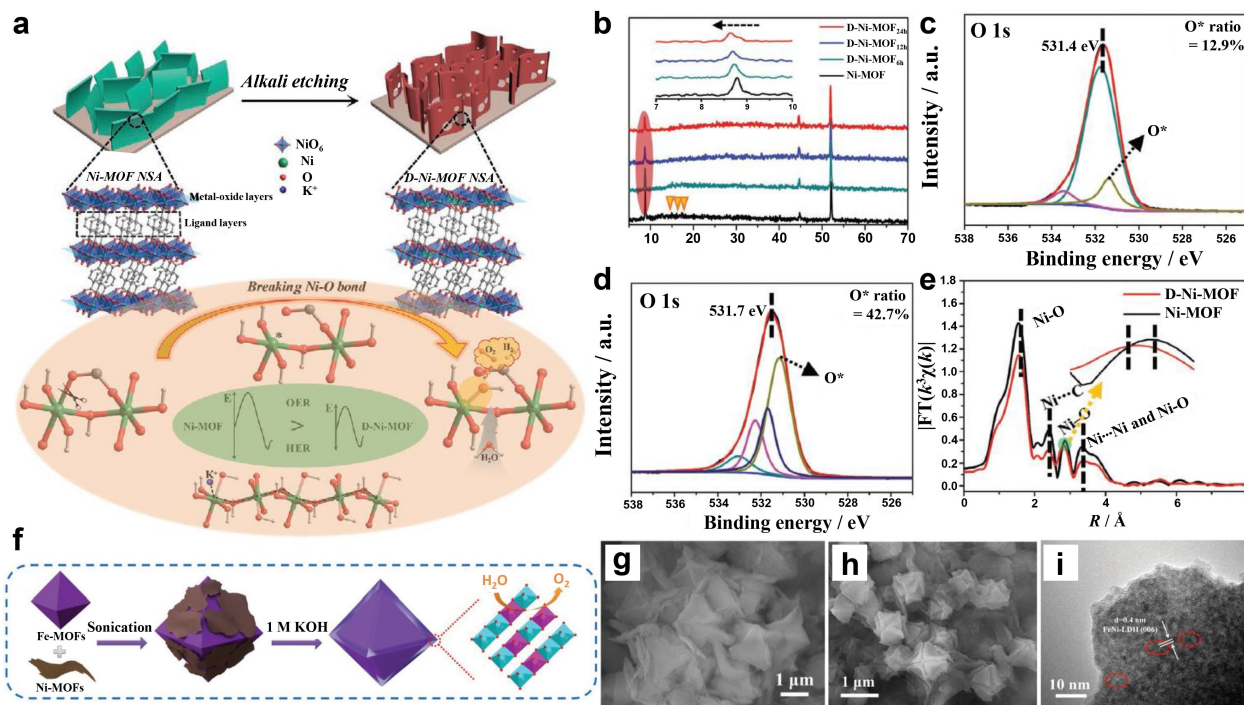


Figure 3. a) Schematic illustration of fabricating defect-rich Ni-MOF nanosheet array (D-Ni-MOF NSA). b) The XRD variations of Ni-MOF NSA along with the alkali etching time. c and d) XPS of O 1s spectra in Ni-MOF and D-Ni-MOF. e) Fourier-transformed $k^2\chi(k)$ EXAFS of Ni-MOF and D-Ni-MOF. Reproduced with permission from Ref.: [54]. Copyright 2020, Wiley-VCH. f) Schematic of the derivatization process leading to Fe-MOFs@Ni-MOFs (FN-2). g and h) SEM images of FN-2 and FN-2i. i) TEM image of FN-2i. Reproduced with permission from Ref.: [55]. Copyright 2019, Wiley-VCH.

form, Bu and co-workers systematically investigated the active species and reaction mechanisms.^[55] Their results demonstrated that most organic ligands in MOFs were replaced by OH⁻ ions in alkaline electrolyte, leading to the generation of NiFe-LDH (Figure 3f) (LDH: layered double hydroxides^[59]). The derived NiFe-LDH acts as the active species during water oxidation. Especially, the conspicuous differences in morphology noticed in the SEM and TEM images alluded to the reconstruction of the mixed Fe-MOFs@Ni-MOFs after alkaline hydrolysis (Figure 3g). The distinct nature of lattice fringes assuredly manifests the existence of metal hydroxides in the MOF derivatives, featuring a lattice spacing of 0.24 nm, which corresponds to the (006) facet of FeNi-LDH.

Attentively, albeit alkaline hydrolysis could partially or completely destroy MOF structures, accurate information on the post-destruction phases *vis-à-vis* during (and/or after) the OER remains missing. Multiple reports also demonstrated that some MOFs displayed relatively high stability over a short period of the alkali immersion treatment.^[55,60] Such a conjecture in terms of the relationships between the real active sites in MOF-derived catalysts and the pristine MOFs needed to be resolved. Resorting to CV and amperometry measurements, Lee and co-workers comprehensively discussed the structural and morphological transitions in ZIF-67.^[56] As shown in Figure 4a, ZIF-67 undergoes a two-step phase evolution (ZIF-67 → α -Co(OH)₂ → β -Co(OH)₂) during the electrochemical treatment (CV, LSV, etc.), accompanied by ligand substitution. During the pre-catalytic treatment, CV profile for the ZIF-67 electrode is measured within different potential windows of 0.925–1.325 V and 0.925–

1.525 V, as shown in Figure 4b. With an increasing number of CV cycles at the potential window of 0.925–1.325 V, two recognizable redox peaks can be observed until the 40th cycle, corresponding to the reversible redox transition between Co²⁺ and Co³⁺ species.

Notably, two redox peaks with half-wave potentials set at 1.049 V and 1.124 V are attributed to α -Co(OH)₂ and β -Co(OH)₂, respectively. After the 40th cycle, the redox peak of α -Co(OH)₂ gradually disappeared. The CV curve at the larger potential window of 0.925–1.525 V shows a new anodic peak. This peak located at 1.330 V is attributed to the oxidation of Co³⁺ to Co⁴⁺. More *In-situ* spectroelectrochemical studies were further used to explore the pre-catalytic transition of Co species in ZIF-67 (Figure 4c). At the low potentials, UV-vis spectra of ZIF-67 show an uprising absorption (< 400 nm) corresponding to the 2-methylimidazole ligands. With the increasing applied potential, the decreased above absorption verifies the leaching of ligands. More obvious changes can be observed from the absorption in the region of 500 to 600 nm, where three representative peaks of tetrahedral Co sites are located at 540, 566, and 587 nm, respectively. At higher applied potential, these absorption peaks of tetrahedral Co sites gradually weaken and disappear at 1.525 V, suggesting the destruction of tetrahedral coordination units in MOFs. Furthermore, *In-situ* Raman spectroelectrochemistry shows a similar derivatization process for ZIF-67 during the CV cycle. Specifically, the Raman peaks stemmed from the ligands gradually vanish with the increasing applied potential. On the other hand, the peak at 522 cm⁻¹ implies the generation of α -Co(OH)₂, and its four-

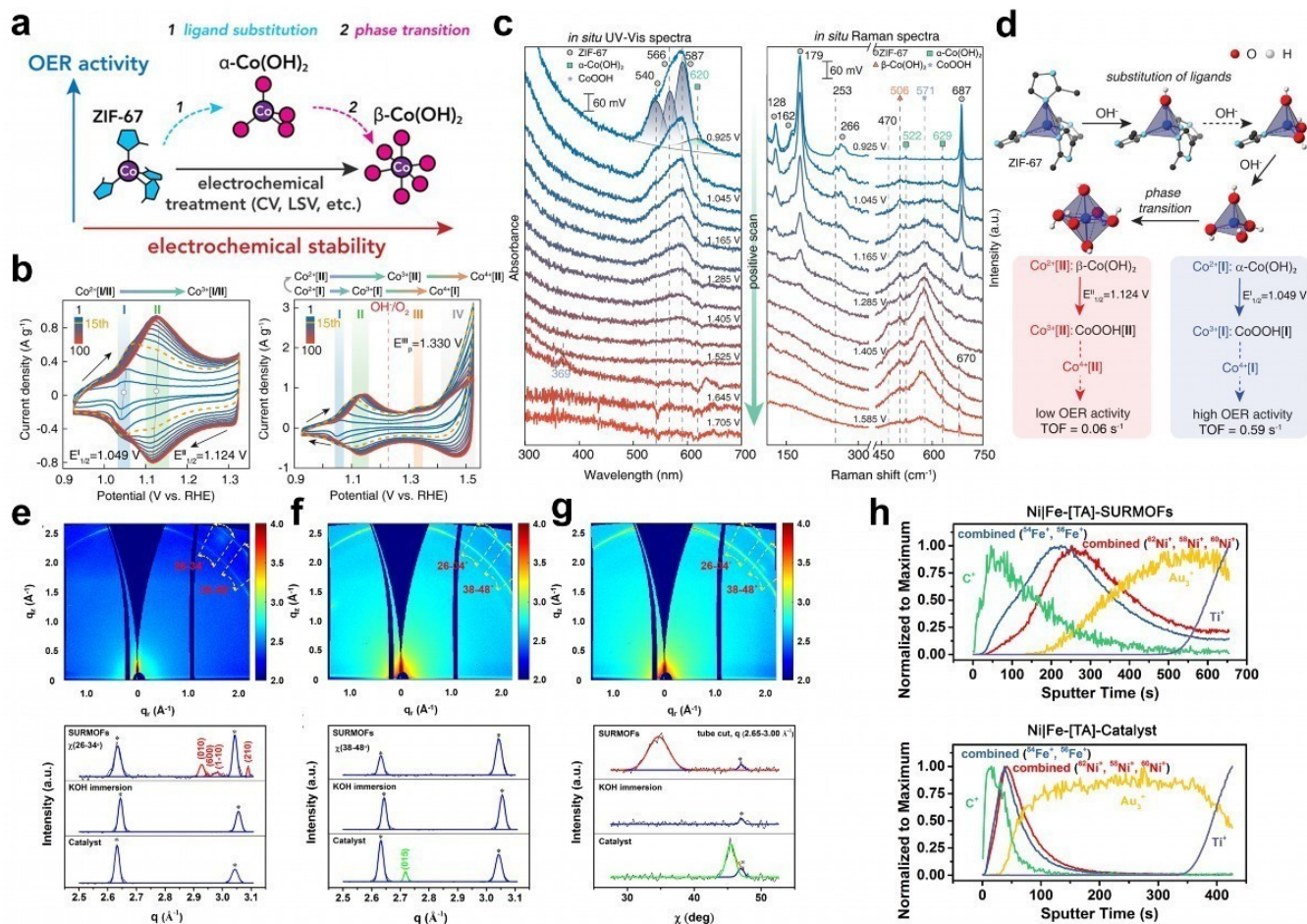


Figure 4. a) The evolution of ZIF-67(Co) under electrochemical treatment. b) CV cycling of ZIF-67@carbon fiber paper at two different potential windows. c) *In situ* UV-vis and *In situ* Raman spectroelectrochemical studies for ZIF-67. d) Mechanism illustration of the electrochemical conversion of ZIF-67 to α -Co(OH)₂ and β -Co(OH)₂. Reproduced with permission from Ref. [56]. Copyright 2020, American Chemical Society. e-g) Grazing-incidence wide-angle X-ray scattering (GIWAXS) data of SURMOFs in the as-prepared state, after 3 min KOH immersion and after OER measurements. In e and f, the cake cuts are obtained at angle regions of $\chi = 26\text{--}34^\circ$ and $38\text{--}48^\circ$, respectively. In g, the tube cuts are performed in a q range of $2.65\text{--}3.00$ Å⁻¹. h) The depth profiles of C⁺, Fe⁺, Ni⁺, Au³⁺ and Ti⁺ secondary ions in Ni|Fe-[TA]-SURMOFs and Ni|Fe-[TA]-Catalyst. All data are obtained with a time-of-flight secondary ion mass spectrometry (ToF-SIMS). Reproduced with permission from Ref. [57]. Copyright 2021, Wiley-VCH.

coordinated bonds around Co sites are confirmed by the peak at 253 cm⁻¹. When the applied potential increases from 0.925 to 0.985 V, the fresh peak arising at 506 cm⁻¹ belongs to the β -Co(OH)₂. This result provides evidence in terms of the phase transition of α -Co(OH)₂ to β -Co(OH)₂. Mechanism of the electrochemical conversion of ZIF-67 to α -Co(OH)₂ and β -Co(OH)₂ are also illustrated in Figure 4d.

In fact, the flexible reconstruction of MOFs in the alkaline electrolyte during the electrochemical measurement complicates the investigation of the evolution mechanism.^[63] Recently, our group has employed the heterostructured NiFe-based surface-mounted MOFs (Ni|Fe-[TA]-SURMOFs) to elucidate the structural and compositional variants during both alkaline immersion and the electrochemical measurements.^[57] As shown in Figures 4e-g, grazing-incidence wide-angle X-ray scattering (GIWAXS) technique was the first time to be used for the study of MOF evolution. In the 2D GIWAXS patterns and the corresponding line-cut and tube-cut profiles, the crystal phase of Ni|Fe-[TA]-SURMOFs can be determined with these diffrac-

tion spots and Bragg peaks. However, the crystalline structures of SURMOFs are destroyed after 3 min KOH immersion treatment, since no diffraction spot and Bragg peak can be detectable. After the OER test, a fresh Bragg peak at $q = 2.72$ Å⁻¹ matches well with the (015) diffraction peak of NiFe-LDH. These results indicate that MOF evolution should include two continuous processes: 1) phase transition of the crystalline SURMOFs into the amorphous metal hydroxides in KOH electrolyte; 2) electrochemical activation and conversion of the amorphous metal hydroxides to low crystalline NiFe-LDH during the CV cycling. More interestingly, a finding with respect to the redistribution of active species in MOFs during the derivatization process declares the self-reconstruction of heterostructured SURMOFs. This was detected utilizing an advanced time-of-flight secondary ion mass spectrometry (ToF-SIMS) instrument. As shown in in-depth profiles (Figure 4h), with the increasing of sputter time (oxygen plasma), Fe⁺ signal can be detected earlier than Ni⁺ signal in the pristine SURMOFs, suggesting the good agreement with the design concept of the heterostruc-

ture. In contrast, Ni- and Fe-species in the Ni|Fe-[TA]-Catalyst (after OER) display a relatively uniform distribution. This data further reinforces the hypothesis of self-reconstruction.

Despite extensive research on alkali etching, realities of the latent MOF derivatization mechanisms and uncontrolled conversion processes impede their transition along higher technological readiness levels,^[64] a cornerstone for commercial adoption.^[65] Of particular importance is to develop versatile and precise methods for the design of high-performance MOF-based catalysts. Apart from the alkali etching, multiple recent studies demonstrate the advantages of etching other cations or anions, such as S^{2-} , Ni^{2+} , Fe^{3+} , Co^{2+} , and so on.^[62,66] Currently, transition metal chalcogenides have fast-tracked research interest in the form of efficient water splitting catalysts due to their appropriate electronic states and high electrical conductivities.^[67] Given the unique morphology and atomically dispersed metal sites, MOFs provide an ideal template for preparing chalcogenide-based OER catalysts. For example, Luo and co-workers developed a facile method to fabricate Co_3S_4 /EC-MOF-based hybrid electrocatalysts.^[61] In Figure 5a, metal hydroxyl fluorides were first prepared solvothermally, showing an echinops-like architecture. Afterward, a universal vapor-phase approach was utilized to grow well-aligned MOFs basing

upon the sacrificial template of metal hydroxyl fluorides. Finally, a vulcanization reaction promoted the conversion of the facial MOFs into metal sulfides, *i.e.*, the Co_3S_4 /EC-MOF hybrids. Both Co_3S_4 and EC-MOF in Co_3S_4 /EC-MOF catalysts are detectable in the XRD patterns (Figure 5b). Moreover, the holistic echinops-like morphology and sheet-like Co_3S_4 species are further confirmed by SEM and TEM images, as shown in Figures 5c–e. Notably, Co_3S_4 /EC-MOF hybrid produced through the controlled surface vulcanization reaction with Na_2S achieves an excellent OER performance, thanks to a mealy overpotential of 226 mV at the current density of 10 mA cm^{-2} . Additionally, cation-etching methods greatly increase the diversity of MOF-derived catalysts. In the aqueous/ethanolic reaction solution, there is a hydrolysis equilibrium for the newly added metal salts, accompanied by proton generation. When MOF crystallites get dissolved in the etchant solution, the H^+ produced from metal salts' hydrolysis destruct the MOF coordination bonds, releasing organic ligands and metal ions.^[49] These released metal ions can react with the external metal ions to generate binary metal hydroxides at the interface of MOFs and electrolytes. In turn, the consumption of protons promotes the aforementioned hydrolysis equilibrium, affording more protons. As shown in Figure 5f, Co-MOF nanoarrays were synthesized on a 3D

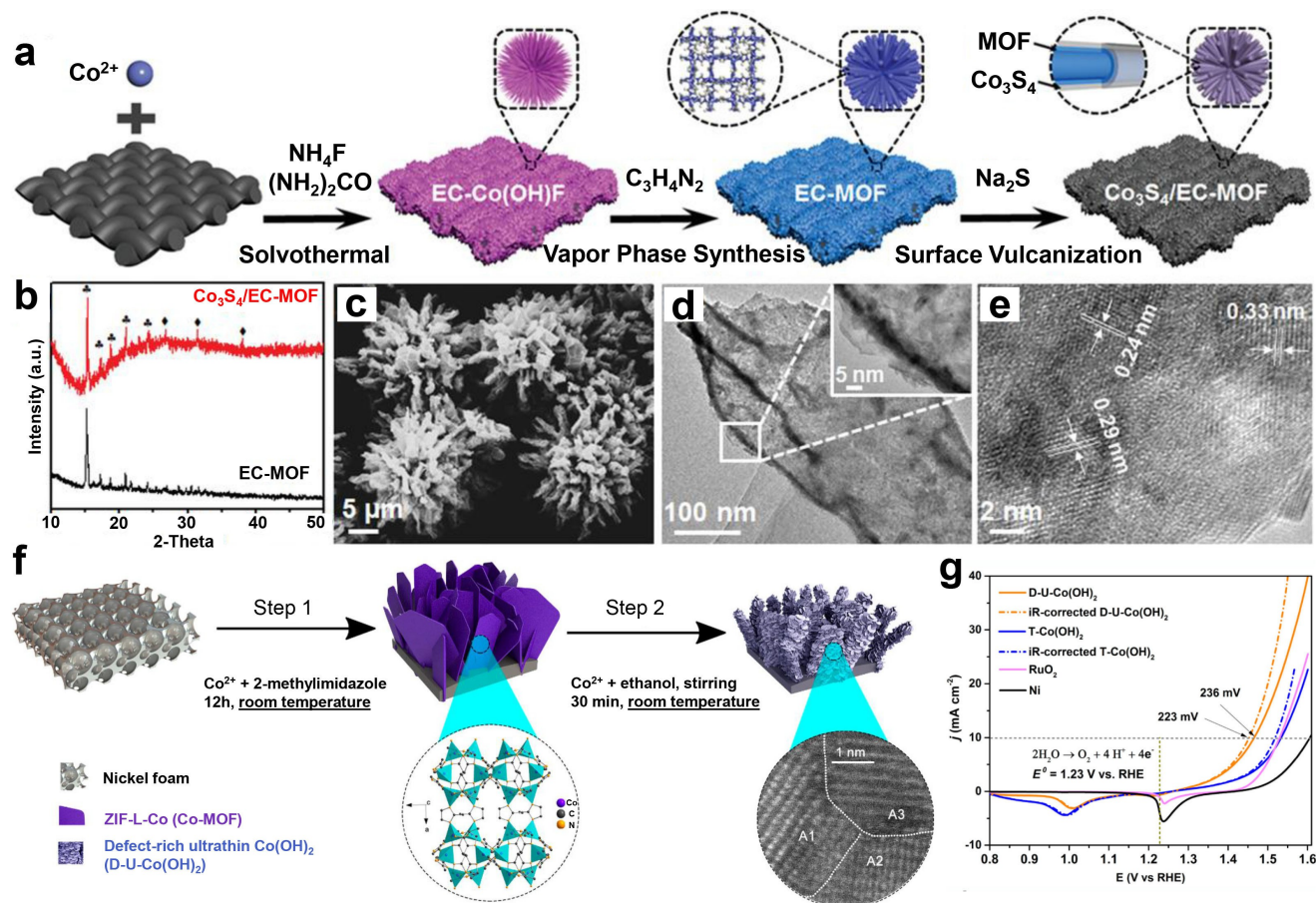


Figure 5. a) Schematic representation of the synthetic route of Co_3S_4 /echinops-like Co-based MOF (Co_3S_4 /EC-MOF). b) XRD patterns of EC-MOF and Co_3S_4 /EC-MOF. c) SEM image, d) TEM image, e) HRTEM image of Co_3S_4 /EC-MOF. Reproduced with permission from Ref. [61]. Copyright 2019, Wiley-VCH. f) The preparation of Co-MOF and defect-rich ultrathin $Co(OH)_2$ (D-U- $Co(OH)_2$). g) Polarization curves of D-U- $Co(OH)_2$ and other reference electrocatalysts. Reproduced with permission from Ref. [62]. Copyright 2019, American Chemical Society.

conductive nickel foam, followed by the conversion of Co-MOF into defect-rich ultrathin Co(OH)₂ (D–U-Co(OH)₂) through *In-situ* etching reaction with Co²⁺ at room temperature.^[62] Furthermore, the MOF-derived D–U-Co(OH)₂ reveals a high OER activity, much superior to the as-prepared thick Co(OH)₂ as well as the commercial RuO₂.

3.1.2. MOF and MOF derivatives for HER: representative examples

3.1.2.1. Mechanisms of HER

HER, like OER, is an integral part of water electrolysis, affording high purity hydrogen. However, catalysts usually exhibit remarkably higher exchange current densities as the HER has fewer reaction steps, and binding energies of reaction intermediates can be tailored more easily. The reaction pathway consists of two steps. In the acidic medium, a proton first adsorbs on the surface of the catalyst (*) in the Volmer step:



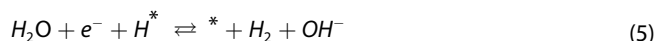
Subsequently, the adsorbed proton reacts either in the so-called Heyrovsky step with another proton from the electrolyte to form a hydrogen molecule:



or two protons adsorbed on the catalyst surface combine in the so-called Tafel step to form a hydrogen molecule which subsequently desorbs:



In alkaline media, the Tafel mechanism remains unchanged. However, due to the low proton concentration in the electrolyte, the Volmer and Heyrovsky steps are associated with water dissociation.



To identify the reaction mechanism and the rate determining step (RDS), the Tafel slope is often studied. The Tafel slope b denotes the potential difference at which the measured Faradaic HER current increases tenfold. In general, the measured overpotential η is often approximated by the equation $\eta = b \bullet \log \frac{j}{j_0}$, where j_0 is the exchange current density. Thus, the parameter b can be easily read as the slope when plotting the (over)potential against the logarithmic current density. In case the proton adsorption/water dissociation (in the alkaline electrolyte) is fast, and the RDS is the Tafel step, *i.e.*, the combination of the adsorbed protons with chemical desorption, one should observe a Tafel slope of $b = 2.3 \frac{RT}{2F} = 29 \text{ mVdec}^{-1}$.

If electrochemical desorption via Heyrovsky mechanism is the RDS, a higher Tafel slope of $b = 4.6 \frac{RT}{3F} = 39 \text{ mVdec}^{-1}$ is expected. Otherwise, the Volmer step may limit the reaction, *i.e.*, by slow proton adsorption or water dissociation. According to the theory, this is reflected by a Tafel slope of

$$b = 4.6 \frac{RT}{F} = 116 \text{ mVdec}^{-1}.$$

Note that R and F are the gas and Faraday constant, respectively and that Tafel slopes are estimated for a temperature $T = 25^\circ\text{C}$.^[68]

It should be further mentioned that although the HER is a relatively simple reaction, it is still not completely understood. Specifically, non-Tafel dependencies, misinterpretations of pseudo-Tafel slopes,^[69] and unexpected pH effects are frequently observed.^[70]

Especially in acidic media, platinum is an excellent catalyst for HER. An ideal catalyst would bind protons only ~ 0.1 eV weaker than the Pt(111) surface, which explains its high activity.^[71] Top-notch electrochemical stability in alkaline and acidic electrolytes are appreciated even more, particularly for technical applications, *e.g.*, PEM electrolyzers. Therefore, especially in an acidic medium, Pt is considered as the benchmark to compare other catalysts. However, it is known that although the activity of Pt electrodes is significantly lowered in alkaline electrolytes. Modifications of the surface with nickel or nickel-iron clusters have proven to relativize this effect, presumably by promoting the water dissociation step.^[72] However, the high prices due to the limited availability of Pt make their replacement with cheaper substitutes very attractive. MOFs and their derivatives received significant attention as HER catalyst in the last decade.^[73]

3.1.2.2. HER active MOFs

The application of MOFs as HER electrocatalysts has advanced beyond classical pyrolysis and calcination treatments. A few select methods also preserve the MOF structures partially. In some cases, MOFs can also find direct use, upon deposition, as HER catalysts. For example, Y. Xu and co-workers recently prepared a highly active NiRu-based binary MOF: Ru-doped Ni₂(BDC)₂TED MOF on a nickel foam and carbon cloth substrate (H₂BDC: 1,4-benzenedicarboxylic acid or terephthalic acid).^[73] This MOF was synthesized using a facile solvothermal method.

As evident from the SEM images shown in Figures 6a and 6b, the MOF film consists of vertically aligned nanosheets, which leads to a significant increase in the electroactive surface area. The individual nanosheets showed a lateral size of $\sim 2 \mu\text{m}$ and a thickness of ~ 10 nm. XPS studies confirm the presence of C, O, N, Ni, Ru in the final MOF film. Compared to a MOF prepared without Ru, the Ni peak is observed with a slight shift, indicating Ru incorporation in the Ni MOF. Further evidence supporting this could be found in the XRD diffractograms. Here, a small lattice distortion of the parent Ni–MOF structure was observed, which is likely caused by the formation of a binary

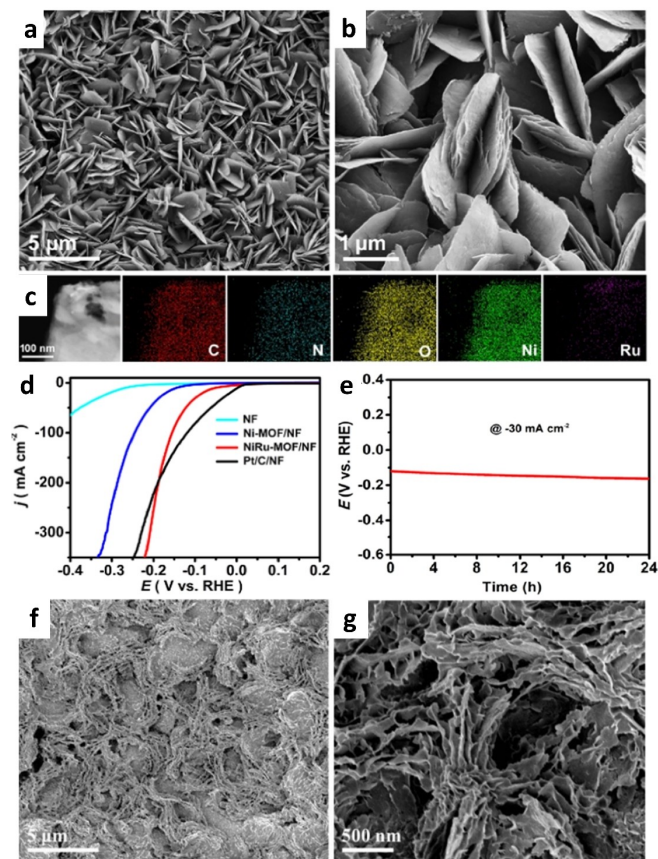


Figure 6. NiRu-based MOF: a) SEM images after synthesis. b) SEM images after preparation, with higher magnification. c) HAADF-STEM with corresponding elemental mapping images. d) Polarization curves for plain Nickel foam substrate (NF), a Ni-MOF/NF reference sample, the as synthesized NiRu-MOF on nickel foam and a Pt/C catalyst also supported on Nickel foam. e) Chronopotentiogram of NiRu-MOF/NF in 1.0 M KOH at a cathodic current density of 30 mA cm^{-2} . f), g) SEM images after degradation tests. Adapted with permission from Ref. [73]. Copyright 2020, American Chemical Society.

NiRu-based MOF structure. The HAADF-STEM elemental mapping (Figure 6c) shows that the elements are uniformly distributed in the MOF as expected. Moreover, a Ru/Ni atomic ratio of $\sim 6/94$ was determined from EDX and ICP-MS. Furthermore, it was discovered that the wettability of the MOF film increased significantly compared to the untreated substrate. This can generally increase the electrochemically active surface area (ECSA) as a larger part of the surface can get wet with the electrolyte. The HER activity was finally investigated in a 1 M KOH solution and compared to that of a commercial platinum on carbon catalyst (Pt/C) (Figure 6d).^[73]

The polarization curve of the NiRu-MOF film shows lower current densities compared to Pt/C, at overpotentials lower than 190 mV. Interestingly, this trend reverses at overpotentials > 200 mV and the MOF outperforms the Pt/C catalyst. However, this is not due to better HER reaction kinetics but due to the fact that the surface of the Pt/C catalyst is partially blocked by the evolving hydrogen, decreasing its effective ECSA. This effect is reduced for the MOF film due to its higher hydrophilicity. Therefore, the surface remains largely free and can contribute to the reaction. Though, this effect is likely to be less

pronounced in technical applications such as electrolyzers, since the gas phase is discharged through the gas diffusion layer, and thus, a Pt/C catalyst is also less susceptible to blocking by the hydrogen produced during the HER. In general, this MOF shows a very high HER activity. For example, an overpotential of 51 mV and 156 mV is reported for a current density of 10 mA cm^{-2} and 100 mA cm^{-2} , respectively.^[73] It should be noted, however, that the current was not normalized on the ECSA, but on the geometric area of the nickel foam used. This can be orders of magnitude smaller. Tafel slope was determined as 90 mV dec^{-1} , which led the authors to conclude that the reaction proceeds via the Volmer Heyrovsky mechanism.^[73] In fact, the slope suggests that the Volmer mechanism is limiting. However, the situation is too complex to show without further measurements that the Heyrovsky mechanism occurs without contributions from the Tafel mechanism.

Since the MOF film was used directly as a catalyst for the HER without prior conversion, the stability of the film is an important issue. When storing the MOF in water for several days, no significant conversion or degradation was detected by XPS, XRD, and SEM. Furthermore, a degradation experiment was performed, where the sample was immersed in 1 M KOH and exposed to a constant current density of 30 mA cm^{-2} for 24 h. Figure 6e shows that the overpotential increased only slightly. Furthermore, by XPS and HAADF-STEM elemental mapping, it was found that the elemental composition remained largely unchanged. However, in the SEM shown in Figures 6f and 6g, a significant change compared to the initial state is visible (Figure 6a versus Figure 6b). This could be due to a partial transformation of the film, for example, by partial leaching of organic linkers, which causes the structure to partially collapse. Nevertheless, the high activity is largely preserved, which makes the work of Y. Xu and co-workers an excellent example of highly active MOFs, which remain largely unchanged even after prolonged use and show only minor morphological transformations. Furthermore, this work pays special attention to an important aspect, the hydrophilic properties of MOFs, which can be beneficial properties for certain applications.

Of course, there are also other examples of direct usage of MOFs as HER catalyst. For instance, it was recently shown by R. Nivetha and co-workers that the large-pore iron(III) carboxylate MIL-100(Fe), which has been known for more than a decade,^[74] could also be directly used as a low-cost HER catalyst.^[75] Lately, also a quick method for the electrochemical synthesis of a NiBTC/Ni MOFs at room temperature has also been demonstrated. This MOF can be used directly as a HER electrocatalyst in both acidic and alkaline media.^[76]

3.1.2.3. Conversion of MOFs in HER catalysts

Due to low conductivity, it is often unavoidable to convert the MOFs. However, the controllability of the conversion and the tunability of the final product are significant advantages for the detailed analysis of active sites and optimization of catalyst design. W. He and co-workers have recently demonstrated a

route for controlled electrochemical conversion of MOFs to amorphous metal sulfides.^[67b] This was demonstrated on two different commonly encountered MOF films, namely ZIF-67 and Fe-MIL-88. H3BTC-modified (1,3,5-benzenetricarboxylic acid) FTO was chosen as the conductive, transparent substrate. Hereupon, MOF films were deposited and subsequently electrochemically converted into amorphous metal sulfides using an electrolyte of 0.1 M KCl and 0.5 M thiourea by potential cycling as shown in Figure 7a. For the ZIF-67, the potential was cycled in the range -1.76 and $+0.15$ V versus Ag/AgCl reference electrode, as can be seen in Figure 7b. Different scan rates were tested. A clear influence of the scan rate on the morphology of the MOF-derived film could be shown. At the relatively high scan rate of 500 mV/s, the morphology of $\text{CoS}_x(0.5)$ remained

largely unchanged, but additional nanosheets were formed on the surface, shown in Figure 7c. As can be seen in Figure 7d, a reduction of the scan rate to 200 mV/s caused the nanosheets to form a highly porous 3D structure denoted as $\text{CoS}_x(0.2)$. A further decrease of the scan rate to 20 mV/s ($\text{CoS}_x(0.02)$) leads to a complete loss of the initial morphology and a rather compact film Figure 7e. Best results were achieved by stepwise decreasing scan rates from 200 to 20 mV/s. As seen in Figure 7f, this results in even larger nanosheets, further increasing film porosity of $\text{CoS}_x(0.2-0.02)$. Furthermore, a decrease of film mass was detected during the electrochemical conversion by electrochemical quartz crystal microbalance (EQCM). This was attributed to the dissolution of the 2-MI ligands. Analysis of XRD, FT-IR, XPS, and Raman spectroscopy data revealed that the Co^{2+} ions in ZIF-67 transform into amorphous cobalt sulfide a-CoS_x , while the 2-MI ligands are released, and thiourea serves as a sulfur source. Moreover, in this process, the OH^- concentration plays a decisive role. During conversion, the potential is cycled in the HER regime (Figure 7b). Due to the low proton concentration (at neutral pH), the HER proceeds partially via the alkaline pathway (comparing reactions 4 and 5). Hence, especially at higher overpotentials, OH^- ions are formed. These hydroxide ions hydrolyze thiourea, releasing S^{2-} ions, which in turn replace the 2-IM ligands in ZIF-67, as shown in Figure 7a. In this way, the dynamic potential curve influences the local OH^- concentration at the electrode and, therefore, the conversion process. This allows fine-tuning of S^{2-} content and porosity by adjustment of potential cycling parameters.

Finally, the electrocatalytic HER properties of the different a-CoS_x films were investigated at neutral pH, as shown in Figure 7g. They were further compared with activities measured of the plain substrate, a platinum film, and a standard CoS_x film which was deposited electrochemically. Obviously, Pt shows the highest and the bare substrate almost zero HER activity. Among the cobalt sulfide films, $\text{CoS}_x(0.2-0.02)$ -12 showed the highest activity followed by the thinner $\text{CoS}_x(0.2-0.02)$, $\text{CoS}_x(0.02)$, $\text{CoS}_x(0.2)$ the $\text{CoS}_x(0.5)$ and finally, the standard CoS_x film. This trend was explained by the difference in porosity and proportion of S_2^{2-} species in the film. To examine the latter, the S_2^{2-} fraction was compared to the overpotentials for different films, as shown in Figure 7h. A direct correlation was observed. This fits with previous studies that identified the S_2^{2-} species acting as active sites for the HER.^[77]

W. He and co-workers showed that the Tafel slopes range from 76 to 109 mVdec⁻¹ for the different films. This cannot be assigned to a single rate-determining reaction step, which is not surprising as in the neutral pH of PBS electrolyte even acidic and alkaline pathways of HER can occur in parallel. The general applicability of this approach for MOFs was demonstrated by the application to Fe-MIL-88, which was successfully transformed into FeS_x .

The main advantages of this method are the simple but reproducible and finely tuneable transformation which can likely be transferred to other MOFs. Since the method is dependent on the local OH^- concentration, a different diffusion behavior can additionally be used to influence the electrochemical MOF transformation.

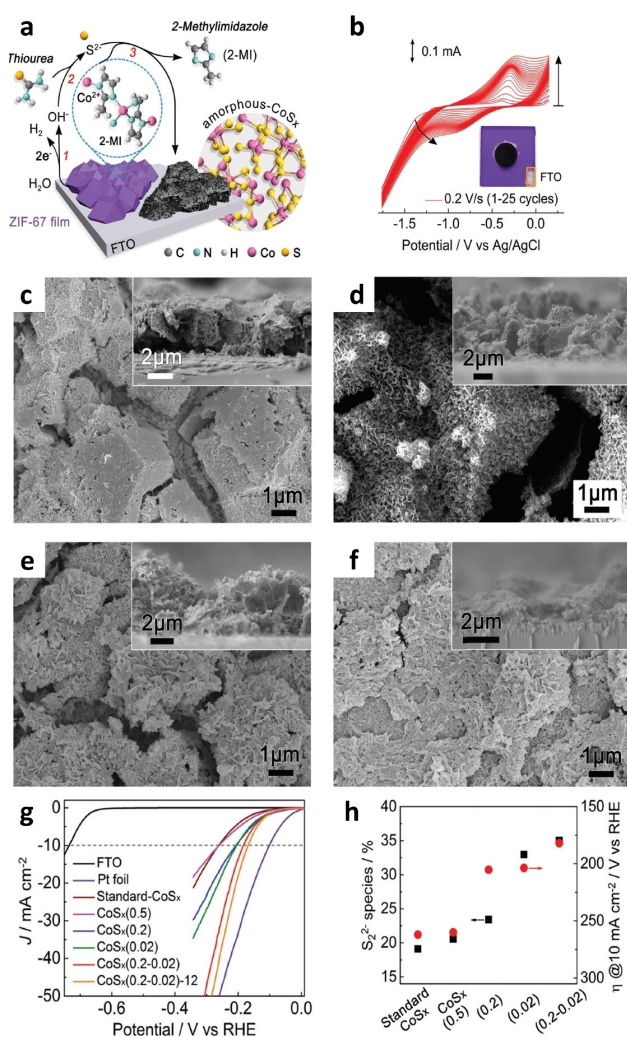


Figure 7. Electrochemical conversion of ZIF-67 (EC-MOF) films into amorphous CoS_x . a) Schematic illustration of the mechanism. b) Cyclic voltammograms during the electrochemical transformation. The initial 25 cycles are shown, and a scan rate of 200 mV was applied. Inset shows the film prior to (purple) and after the transformation (black region). SEM images of c) $\text{CoS}_x(0.5)$, d) $\text{CoS}_x(0.2)$, e) $\text{CoS}_x(0.02)$, f) $\text{CoS}_x(0.2-0.02)$. Insets show typical cross sections. g) Polarization curve of the as-prepared a-CoS_x samples, performed in 1 M PBS buffer solution (pH = 7) at a scan rate of 5 mV s^{-1} . h) Correlation between percentage of S_2^{2-} and electrochemical activity. Adapted with permission from Ref. [67b]. Copyright Wiley and Sons 2018.

3.2. MOF based electrocatalysts for oxygen electro-reduction

The electro-reduction of oxygen is of high importance for various energy conversion systems such as fuel cells and metal-air batteries.^[78] So far, only Pt-based catalysts have shown sufficient catalytic activity and stability.^[79] Recently, there has been much attention on developing MOF-based electrocatalysts towards ORR, owing to their easily tuneable structure and composition.^[80] First of all, it should be noted that there are several fundamental requirements for an efficient ORR catalyst. First, the catalyst material needs to be electrically conductive. Second, for good catalytic performance, the binding energy of ORR intermediates to the active sites needs to be neither too strong nor too weak.^[37,81] Third, the catalyst needs to be stable in the potential range of 0.1–1.0 V vs RHE at which the ORR takes place in aqueous electrolytes.

Currently, there are two main strategies for the usage of MOF-based ORR electrocatalysts, namely, pyrolyzed and unpyrolyzed. The focus of this section is set on the studies utilizing unpyrolyzed MOF-based ORR electrocatalysts. Unpyrolyzed MOF-based ORR electrocatalysts can be divided into the following subgroups: utilization of pristine conductive MOFs directly as the electrode, MOFs decorated with active species/clusters/nanoparticles, MOFs integrated/mixed with other conductive materials such as carbon.

Considering conditions above, several MOF-based materials have been utilized as ORR catalysts. For instance, conductive MOF with nickel centers, $\text{Ni}_3(\text{hexaiminotriphenylene})_2$ ($\text{Ni}_3(\text{HITP})_2$), has shown promising activities in alkaline solutions.^[23c] The ORR polarization curves are shown in Figure 8a. The electrocatalytic performance of $\text{Ni}_3(\text{HITP})_2$ is clearly seen in the presence of O_2 ; see the red curve in Figure 8a. Theoretical calculations were done to identify the possible active sites, where Ni atom, the nitrogen atoms of imine, or one of the three unique carbon atoms were considered.^[82] The calculations gave the lowest O_2 binding energy to $\beta\text{-C}$ near the imine groups, as illustrated in Figure 8b. Another study investigated the ORR performance of metal-catecholates (M-CATs, $\text{M}=\text{Ni}$ or Co), hexahydroxytriphenylene (HHTP: 2,3,6,7,10,11-hexahydroxytriphenylene) linked with transition metal ions ($\text{Ni}(\text{II})$ and $\text{Co}(\text{II})$).^[83] In that study, the M-CATs were mixed with carbon black for the electrocatalytic activity measurements. The ORR activities for both of the M-CATs were promising. The authors indicated that $\text{M}-\text{O}_6$ coordination sites are the likely active sites for ORR. These studies highlight the promising application of conductive MOFs as ORR catalysts which is in its infancy.

Recently, ZIF-8 has been used as the template in the preparation of Pt nanoparticles with ~ 1 nm diameter.^[84] The schematic of the Pt_{12} clusters inside the ZIF-8 and subsequent dissolution of the MOF in an acidic environment leaves ultra-small Pt nanoparticles with ~ 1 nm diameter on the substrate, schematically shown in Figure 8c. Such Pt nanoparticles have shown twice higher ORR activity compared to the commercial Pt/C catalyst. In another study, the Cu-MOF was mixed with CuS nanoparticles, where authors prepared various amounts of CuS nanoparticles (nano-CuS) in/on a 3D Cu-MOF,

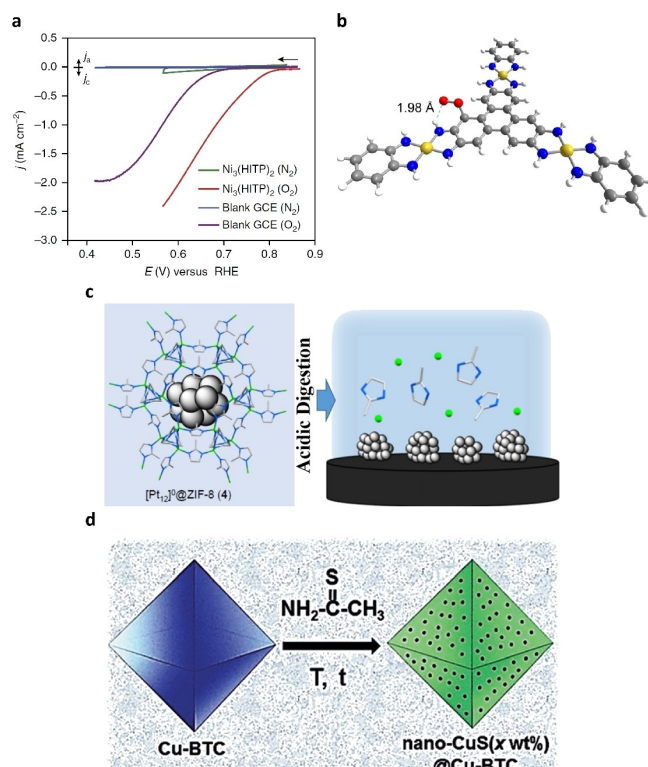


Figure 8. a) The ORR polarization curves of $\text{Ni}_3(\text{HITP})_2$ in N_2 saturated (green) and O_2 saturated (red) 0.1 M KOH electrolyte. Polarization curve of glassy carbon electrode (GCE) in N_2 and O_2 saturated (blue and purple, respectively) 0.1 M KOH solutions are shown for comparison. The working electrodes were rotated at 2000 r.p.m. and scan speed was set to 5 mV/s. Adapted with permission from Ref. [23c]. Copyright © 2016, Springer Nature. b) Simulated image indicating the binding site of O_2 molecules on the $\text{Ni}_3(\text{HITP})_2$. O, Ni, N, C, and H atoms are illustrated in red, yellow, blue, grey, and white colors, respectively. Adapted with permission from Ref. [82]. Copyright © 2017, American Chemical Society. c) A schematic showing the synthesis of Pt nanoparticles using ZIF-8 as a template. The dissolution of the ZIF-8 by protonation in acidic solution results in small Pt nanoparticles on the support electrode. Adapted with permission from Ref. [85]. Copyright © 2019, American Chemical Society. d) Illustration shows the synthesis of CuS nanoparticles (x wt%)@Cu-BTC. Adapted with permission from Ref. [84]. Copyright © 2016, Wiley.

$[\text{Cu}_3(\text{BTC})_2 \cdot (\text{H}_2\text{O})_3]$ (BTC = 1,3,5-benzenetricarboxylate), see Figure 8d.^[84] The electrical conductivity of Cu-MOF increased with the addition of CuS nanoparticles. Particularly, the conductivity increased from 0.17 S cm^{-1} to 1.8 S cm^{-1} when the CuS loading increased from 28 wt% to 56 wt%. Highest onset potential, 0.91 V vs RHE, towards the ORR was observed for 28 wt% CuS loaded Cu-MOF samples. The observed ORR activity was still significantly lower than that of commercial Pt/C catalyst but it provides a new paradigm for the synthesis of MOF-based composite ORR catalyst materials.

3.3. Non-pyrolyzed MOF derivatives for bifunctional electrocatalysis

Exploring active and stable electrocatalysts that enable dual functions, either OER and ORR, or HER and OER, are important for harnessing clean energy in electrolyzers, fuel cells and next-

generation batteries. Whereas a number of pyrolyzed MOF derivatives are known for bifunctionality, a) ORR and OER; b) OER and HER electrocatalysts, developing non-pyrolyzed MOF derivatives for bifunctional electrocatalysis remain understudied.

Design of electrocatalysts with dual functions should meet the well-known Sabatier principle: the binding strength between the catalysts and intermediates should neither be too strong nor too weak.^[86] Following this, Fischer and co-workers reported an electrocatalyst strain modulation approach, leading to highly active bifunctional ORR/OER electrocatalysts based on surface mounted NiFe-BDC MOFs.^[87] In brief, different functional groups such as $-\text{Br}$, $-\text{OCH}_3$, and $-\text{NH}_2$ were introduced to BDC, eliciting defect strain and adjustable binding energies. Results demonstrated that the $-\text{NH}_2$ modified MOF derivatives exhibited high OER activity (current density of 200 mA cm^{-2} at an overpotential of only $\approx 210 \text{ mV}$) in alkaline media across a small overpotential window of $\approx 0.69 \text{ V}$. An outcome of modest binding strength with the intermediates, this OER activity outperformed the then state-of-the-art OER catalysts.

3.4. Non-pyrolyzed MOF derivatives for electrochemical CO_2 reduction

Electrochemical CO_2 reduction reaction comprises two, four, six, and eight electrons transfer reaction paths corresponding to the production of different products, such as carbon monoxide (CO), formic acid (HCOOH), formaldehyde (HCHO), oxalic acid ($\text{H}_2\text{C}_2\text{O}_4$), ethylene (C_2H_4), methane (CH_4), ethanol ($\text{C}_2\text{H}_5\text{OH}$), etc.^[88] The reaction pathways and products of electrochemical CO_2 conversion are mainly dominated by the electrocatalysts.^[91] Generally, ECO2RR covers three stages: a) CO_2 adsorption onto surface; b) combination and transformation of CO_2 into intermediates after electron and proton transfer reactions; c) release of the products.^[92] Briefly, the $\text{C}=\text{O}$ bond in CO_2 could be initially perturbed upon getting adsorbed on the electrocatalyst surface. This, perhaps, has the most profound impact in ECO2RR. Meanwhile, the CO_2 molecules and the electrocatalysts share electrons and protons during ECO2RR, where CO_2 molecules are converted to CO^* and further form COOH^* (or HCO_2^-) in the electron-proton system (* refers to the catalysts/electrode surface sites). If the electrocatalyst surface binds the CO^* weakly and COOH^* strongly, the resulting product is highly likely to be CO. Or else, the other products will be produced from ECO2RR. It is noteworthy that CO_2 molecules tend to form two carbon radical anions (CO_2^-) in aprotic solvents (e.g., *N,N*-dimethylformamide) and further react with another adsorbed CO_2 molecule in non-aqueous systems ($\text{CO}_2^- + \text{CO}_2 \rightarrow \text{O}_2\text{C}-\text{CO}_2^-$). Therefore, aligned with the mechanism aforesaid, designing an electrocatalyst with optimal binding affinity for CO_2^- and COOH^* is a high-reward research frontier.

Akin to other electrocatalysis reactions, MOFs and MOF derivatives have drawn increasing interest from researchers towards the electrochemical conversion of CO_2 . This is particularly expedited by their tunable porosity and amenability to facile electrode preparation.^[10c,93] However, synthesizing MOFs

or MOF derivatives breaking the trade-off between high selectivity and top-notch Faradaic efficiency, remains an uncharted territory. Recently, several reviews have summarized the hitherto known strategies for improving the faradaic efficiency and selectivity of pristine MOFs and MOF derivatives for ECO2RR.^[10c,17a,93–94] Nevertheless, the current MOF derivative-based ECO2RR benchmarks are obtained through pyrolysis.

Reviewing the ECO2RR literature, we find the present research attention to largely revolve around the *In-situ* electrochemical transformations of pristine MOFs to highly active electrocatalysts in 0.5 M KHCO_3 . Depending on the stability, intrinsic composition, and conductivity of the pristine MOFs, two approaches generate highly active species by *In-situ* electrochemical transformations: 1) partial conversion; 2) complete conversion. Considering ECO2RR, for example, a single type of Cu_2O active sites is essential to achieve high CH_4 selectivity. As a proof of concept, Cao and co-workers employed *In-situ* electrochemical transformation to generate a single kind of Cu_2O active sites. This was done by partially reducing the metal nodes of CuHHTP into $\text{Cu}_2\text{O}@CuHHTP$ (Figure 9).^[89] This concept shows the merits of controllable size by engaging several facets to the active sites, sustains optimal conductivity, and stabilizes the intermediates. Results suggest that the $\text{Cu}_2\text{O}@CuHHTP$ prepared by *In-situ* partial electrochemical transformation could demonstrate a CH_4 selectivity as high as 73%. On the other hand, the long-range order and high surface area nature of pristine MOFs enable to create high concentrations of surface metal-based active sites. Nonetheless, the pristine MOFs usually suffer from poor conductivity, restricting their applications in electrocatalysis.

Interestingly, some pristine MOFs exhibit electrochemical instability when subjected to overpotential. Taking this in mind, researchers proposed the strategy of electrified stimuli-based structural rearrangements at certain reducing potentials to fully convert the pristine MOFs to highly active ECO2RR electrocatalysts. Simply put, this strategy was aimed at improving their Faradaic efficiency. By tuning the ligand of the pristine MOFs and reduction potentials, a Faradaic efficiency of 95% is



Figure 9. Schematic illustration of the *In-situ* electrochemical transformation of pristine MOF to obtain MOF derivatives: a) partially conversion; Copyright 2020, Wiley-VCH Verlag GmbH & KGaA, Weinheim; Reproduced with permission from Ref. [89]. b) fully conversion. Copyright 2021, Royal Society of Chemistry. Reproduced with permission from Ref. [90].

achieved in Bi(BTB) (BTB: 1,3,5-Tris(4-carboxyphenyl)benzene) while electrochemically reducing CO₂ to HCOOH. This can further be improved to 98% by utilizing Bi-BDC as the pristine MOF.^[89,97] These results establish the *In-situ* electrochemical method as an efficient paradigm to deliver ECO2RR catalysts with high Faradaic efficiency. However, studies in this area are limited, and only HCOOH and CH₄ have been realized thus far as the reduced commodity chemicals (Table 2). To improve the Faradaic efficiencies and to selectively produce other high-value chemicals (e.g., CH₄, C₂H₄, methanol, ethanol), generalized trends need to evolve. This can perhaps only happen by more intensive research efforts hereafter.

4. Conclusion and Future Outlook

Contextualizing the societal relevance of green energy in a sustainable future, new benchmark electrocatalysts with limited energy demand are the need of the hour. With a steady upswing in new MOFs with just the crystalline frameworks soaring beyond 100,000 structures (Cambridge Crystallographic Data Center MOF collection),^[15,98] their compositional modularity paves the way for bottom-up design and development of highly active electrocatalysts. In this review, we summarize several approaches of harnessing MOFs as electrocatalysts, sharing one common characteristic: these overcome the bottleneck of energy-intensive catalyst preparation (in the form of calcination or pyrolysis).

As regards electrocatalysis, research findings over the last decade have translated into several effective MOF design approaches.^[99] These include fine-tuning of defect chemistry, lattice strain, electronic structure, catalyst crystallite size, electronic and ionic conductivity, among others.^[100] Under this backdrop, to holistically improve the catalytic activities of MOFs, it is beyond time to address the elusive knowledge gaps. Some aspects that preclude a general paucity of comprehension are: a) What is the role of MOFs, the catalyst or pre-catalyst?; b) Where do the active sites originate from?; c) Can we quantitatively, *a priori* correlate structure and electrocatalytic performance parameters? These are burning questions that

future studies have to answer in the pursuit of gaining insights into key factors that preclude translational research in this area.

Aligned with the overarching commitment of translational research in materials chemistry to green and sustainable routes, the development of environmentally benign post-treatment approaches is an alternative, promising for many reasons. Adopting these mild treatments mitigate not only the energy footprint of traditional calcination and pyrolysis treatments but also offer low-cost, greener solutions. In synergy with the determination of catalytically active sites, a critical interrogation of the underlying mechanisms of structural transitions holds the key to unlocking the “real-world” potentials. Many aspects appear interwoven: 1) Top-of-the-line characterization techniques under *In-situ* or *In-operando* conditions should be developed. These include small-angle X-ray scattering (SAXS), X-ray absorption spectroscopy (XAS), small-angle neutron scattering spectroscopy (SANS), X-ray absorption near edge structure (XANES), and isotopic labeling. 2) More efforts need to be invested in the evaluation of material properties before and after electrochemical treatments, disclosing the origin of active species as well as the structure-function relationships. 3) Additionally, utilization of density functional theory provides another way to probe the optimal electrochemical reaction pathways, offering *de novo* design of active sites in MOFs and/or MOF derivatives. This can culminate in a predictive modeling-guided blueprint complemented well by state-of-the-art machine learning approaches.^[101]

With the benefit of hindsight, we envisage that a two-way iterative feedback loop between experimental observations (complemented by machine learning tools) and computational simulations (augmented by machine learning tools) will serve as a strong prognostic indicator,^[102] making headway in handpicking commercialization-ready MOF electrocatalysts.^[65] Our present assessment, herein, not only offers a perspective on the energy-efficient, environmentally benign approaches of developing MOF electrocatalysts (thus avoiding pyrolysis and/or calcination derived carbonized hybrids), it also widely underpins the general understanding of MOF electrocatalysts.

Reflecting upon the diverse pore environments offered by modular families of MOFs and the synthetically tailored versatility while designing them *de novo*,^[103] potentials of MOFs and MOF derivatives (without compromising their framework nature and/or porosity) largely remain unexplored. Moving away from the traditional high-throughput approach of exploring “one-size-fits-all” material solutions, the discovery of reaction-specific and stable electrocatalysts could make swift progress if we critically examine each benchmark MOF electrocatalyst documented thus far, as regards the catalysis mechanisms and active sites’ density regulation are concerned. Paying more attention to energy-efficient and environmentally benign activation routes can only take us closer to the lofty targets set for new-generation electrocatalysts.

Table 2. Non-pyrolyzed MOFs for electrochemical reduction of CO₂.

Pristine MOF	Derivatization approach	Main product	Faradaic Efficiency (%)	Refs.
Bi(btb)	<i>In-situ</i> electrochemical transformation	HCOO ⁻	95	[95]
Bi-TATB (TATB; 1,3,5-triazine-2,4,6-tribenzoic acid)	<i>In-situ</i> electrochemical transformation	HCOO ⁻	96.1	[90]
CuHHTP	<i>In-situ</i> electrochemical transformation (Partially, Cu ₂ O)	CH ₄	73	[89]
Bi ₉ (C ₉ H ₃ O ₆) ₉ (H ₂ O) ₉ (CAI-17)	<i>In-situ</i> electrochemical transformation	HCOOH	95	[96]
Bi-BDC	<i>In-situ</i> electrochemical transformation	HCOO ⁻	98	[97]

Acknowledgements

S.M. is thankful to the generous fellowship grant from the Alexander von Humboldt foundation. S.H. acknowledges financial support from the China Scholarship Council. W.J.L. and R.A.F. appreciate the financial support from Deutsche Forschungsgemeinschaft (DFG) project MOFMOX (FI 502/43-1) and DFG Project 279409724. The authors also acknowledge the financial support from German Research Foundation (DFG) in the framework of the Germany's Excellence Strategy – EXC 2089/1-390776260, cluster of excellence 'e-conversion'. Open Access funding enabled and organized by Projekt DEAL.

Conflict of Interest

The authors declare no conflict of interest.

Keywords: Conductive scaffolds · Electrocatalysis · Metal-organic frameworks · Oxygen evolution reaction

- [1] S. R. Batten, N. R. Champness, X.-M. Chen, J. Garcia-Martinez, S. Kitagawa, L. Öhrström, M. O'Keeffe, M. Paik Suh, J. Reedijk, *Pure Appl. Chem.* **2013**, *85*, 1715.
- [2] a) R.-B. Lin, S. Xiang, W. Zhou, B. Chen, *Chem* **2020**, *6*, 337–363; b) S. Mukherjee, A. V. Desai, S. K. Ghosh, *Coord. Chem. Rev.* **2018**, *367*, 82–126.
- [3] A. Bavykina, N. Kolobov, I. S. Khan, J. A. Bau, A. Ramirez, J. Gascon, *Chem. Rev.* **2020**, *120*, 8468–8535.
- [4] W. P. Lustig, S. Mukherjee, N. D. Rudd, A. V. Desai, J. Li, S. K. Ghosh, *Chem. Soc. Rev.* **2017**, *46*, 3242–3285.
- [5] S. Mukherjee, M. J. Zaworotko, *Trends Chem.* **2020**, *2*, 506–518.
- [6] a) R.-B. Lin, S. Xiang, W. Zhou, Q. Xu, *Adv. Mater.* **2018**, *30*, 1703663.
- [7] B. Moulton, M. J. Zaworotko, *Chem. Rev.* **2001**, *101*, 1629–1658.
- [8] O. M. Yaghi, M. J. Kalmutzki, C. S. Diercks, in *Introduction to Reticular Chemistry*, **2019**, pp. 285–293.
- [9] M. Z. Hussain, Z. Yang, Z. Huang, Q. Jia, Y. Zhu, Y. Xia, *Adv. Sci.* **2021**, *8*, 2100625.
- [10] a) H.-F. Wang, L. Chen, H. Pang, S. Kaskel, Q. Xu, *Chem. Soc. Rev.* **2020**, *49*, 1414–1448; b) X. F. Lu, B. Y. Xia, S.-Q. Zang, X. W. Lou, *Angew. Chem. Int. Ed.* **2020**, *59*, 4634–4650; *Angew. Chem.* **2020**, *132*, 4662–4678; c) W. Li, S. Mukherjee, B. Ren, R. Cao, R. A. Fischer, *Adv. Energy Mater.* 2003499, DOI: 10.1002/aenm.202003499.
- [11] N.-T. Suen, S.-F. Hung, Q. Quan, N. Zhang, Y.-J. Xu, H. M. Chen, *Chem. Soc. Rev.* **2017**, *46*, 337–365.
- [12] M. Shao, Q. Chang, J.-P. Dodelet, R. Chenitz, *Chem. Rev.* **2016**, *116*, 3594–3657.
- [13] S. Jin, *ACS Energy Lett.* **2019**, *4*, 1443–1445.
- [14] The Sustainable Development Goals Report 2021, United Nations, <https://unstats.un.org/sdgs/report/2021/The-Sustainable-Development-Goals-Report-2021.pdf>, accessed on 17th October 2021.
- [15] P. Z. Moghadam, A. Li, X.-W. Liu, R. Bueno-Perez, S.-D. Wang, S. B. Wiggins, P. A. Wood, D. Fairen-Jimenez, *Chem. Sci.* **2020**, *11*, 8373–8387.
- [16] S. Mukherjee, K. K. R. Datta, R. A. Fischer, *Trends Chem.* **2021**, *3*, 911–925.
- [17] a) P.-Q. Liao, J.-Q. Shen, J.-P. Zhang, *Coord. Chem. Rev.* **2018**, *373*, 22–48; b) H. B. Aiyappa, J. Masa, C. Andronescu, M. Muhler, R. A. Fischer, W. Schuhmann, *Small Methods* **2019**, *3*, 1800415.
- [18] Q.-L. Zhu, W. Xia, L.-R. Zheng, R. Zou, Z. Liu, Q. Xu, *ACS Energy Lett.* **2017**, *2*, 504–511.
- [19] L. Wang, Y. Zhu, C. Du, X. Ma, C. Cao, *J. Mater. Chem. A* **2020**, *8*, 24895–24919.
- [20] C. Schneider, D. Ukaj, R. Koerver, A. A. Talin, G. Kieslich, S. P. Pujari, H. Zuilhof, J. Janek, M. D. Allendorf, R. A. Fischer, *Chem. Sci.* **2018**, *9*, 7405–7412.
- [21] S. Zhao, Y. Wang, J. Dong, C.-T. He, H. Yin, P. An, K. Zhao, X. Zhang, C. Gao, L. Zhang, J. Lv, J. Wang, J. Zhang, A. M. Khattak, N. A. Khan, Z. Wei, J. Zhang, S. Liu, H. Zhao, Z. Tang, *Nat. Energy* **2016**, *1*, 16184.
- [22] a) S. Gonen, O. Lori, O. Fleker, L. Elbaz, *ChemCatChem* **2019**, *11*, 6124–6130; b) S. Gonen, O. Lori, G. Cohen-Taguri, L. Elbaz, *Nanoscale* **2018**, *10*, 9634–9641.
- [23] a) Y. Yan, B. Y. Xia, B. Zhao, X. Wang, *J. Mater. Chem. A* **2016**, *4*, 17587–17603; b) J.-D. Yi, R. Xu, Q. Wu, T. Zhang, K.-T. Zang, J. Luo, Y.-L. Liang, Y.-B. Huang, R. Cao, *ACS Energy Lett.* **2018**, *3*, 883–889; c) E. M. Miner, T. Fukushima, D. Sheberla, L. Sun, Y. Surendranath, M. Dincă, *Nat. Commun.* **2016**, *7*, 10942; d) J. Zhou, Y. Dou, A. Zhou, L. Shu, Y. Chen, J.-R. Li, *ACS Energy Lett.* **2018**, *3*, 1655–1661; e) X. Zhao, B. Pattengale, D. Fan, Z. Zou, Y. Zhao, J. Du, J. Huang, C. Xu, *ACS Energy Lett.* **2018**, *3*, 2520–2526; f) L. Jiao, H.-L. Jiang, *Chem* **2019**, *5*, 786–804; g) J. Li, W. Huang, M. Wang, S. Xi, J. Meng, K. Zhao, J. Jin, W. Xu, Z. Wang, X. Liu, Q. Chen, L. Xu, X. Liao, Y. Jiang, K. A. Owusu, B. Jiang, C. Chen, D. Fan, L. Zhou, L. Mai, *ACS Energy Lett.* **2019**, *4*, 285–292.
- [24] a) A. J. Howarth, Y. Liu, P. Li, Z. Li, T. C. Wang, J. T. Hupp, O. K. Farha, *Nat. Rev. Mater.* **2016**, *1*, 15018; b) L. Feng, K.-Y. Wang, G. S. Day, M. R. Ryder, H.-C. Zhou, *Chem. Rev.* **2020**, *120*, 13087–13133.
- [25] V. Artero, M. Fontecave, *Chem. Soc. Rev.* **2013**, *42*, 2338–2356.
- [26] W.-H. Li, J. Lv, Q. Li, J. Xie, N. Ogiwara, Y. Huang, H. Jiang, H. Kitagawa, G. Xu, Y. Wang, *J. Mater. Chem. A* **2019**, *7*, 10431–10438.
- [27] L. Yang, S. Kinoshita, T. Yamada, S. Kanda, H. Kitagawa, M. Tokunaga, T. Ishimoto, T. Ogura, R. Nagumo, A. Miyamoto, M. Koyama, *Angew. Chem. Int. Ed.* **2010**, *49*, 5348–5351; *Angew. Chem.* **2010**, *122*, 5476–5479.
- [28] a) K. S. Mali, N. Pearce, S. De Feyter, N. R. Champness, *Chem. Soc. Rev.* **2017**, *46*, 2520–2542; b) A. Sweetman, N. R. Champness, A. Saywell, *Chem. Soc. Rev.* **2020**, *49*, 4189–4202.
- [29] a) J. Canivet, A. Fateeva, Y. Guo, B. Coasne, D. Farrusseng, *Chem. Soc. Rev.* **2014**, *43*, 5594–5617; b) B. D. McCarthy, A. M. Beiler, B. A. Johnson, T. Liseev, A. T. Castner, S. Ott, *Coord. Chem. Rev.* **2020**, *406*, 213137.
- [30] S. Yuan, L. Feng, K. Wang, J. Pang, M. Bosch, C. Lollar, Y. Sun, J. Qin, X. Yang, P. Zhang, Q. Wang, L. Zou, Y. Zhang, L. Zhang, Y. Fang, J. Li, H.-C. Zhou, *Adv. Mater.* **2018**, *30*, 1704303.
- [31] R. G. Pearson, *J. Am. Chem. Soc.* **1963**, *85*, 3533–3539.
- [32] J. H. Cavka, S. Jakobsen, U. Olsbye, N. Guillou, C. Lamberti, S. Bordiga, K. P. Lillerud, *J. Am. Chem. Soc.* **2008**, *130*, 13850–13851.
- [33] M. Dan-Hardj, C. Serre, T. Frot, L. Rozes, G. Maurin, C. Sanchez, G. Férey, *J. Am. Chem. Soc.* **2009**, *131*, 10857–10859.
- [34] V. Colombo, S. Galli, H. J. Choi, G. D. Han, A. Maspero, G. Palmisano, N. Masciocchi, J. R. Long, *Chem. Sci.* **2011**, *2*, 1311–1319.
- [35] H. J. Choi, M. Dincă, J. R. Long, *J. Am. Chem. Soc.* **2008**, *130*, 7848–7850.
- [36] S. Yuan, J.-S. Qin, C. T. Lollar, H.-C. Zhou, *ACS Cent. Sci.* **2018**, *4*, 440–450.
- [37] S. Hou, R. M. Kluge, R. W. Haid, E. L. Gubanov, S. A. Watzel, A. S. Bandarenka, B. Garlyyev, *ChemElectroChem* **2021**, *8*, 3433–3456.
- [38] Q. Shao, J. Yang, X. Huang, *Chem. Eur. J.* **2018**, *24*, 15143–15155.
- [39] a) Y. Pan, X. Xu, Y. Zhong, L. Ge, Y. Chen, J.-P. M. Veder, D. Guan, R. O'Hayre, M. Li, G. Wang, H. Wang, W. Zhou, Z. Shao, *Nat. Commun.* **2020**, *11*, 2002; b) Y. Zhu, W. Zhou, Z. Shao, *Small* **2017**, *13*, 1603793.
- [40] a) J. T. Mefford, X. Rong, A. M. Abakumov, W. G. Hardin, S. Dai, A. M. Kolpak, K. P. Johnston, K. J. Stevenson, *Nat. Commun.* **2016**, *7*, 11053; b) H. Liu, X. Li, C. Peng, L. Zhu, Y. Zhang, H. Cheng, J. Cui, Q. Wu, Y. Zhang, Z. Chen, W. Zou, W. Gu, H. Huang, J. Wang, B. Ye, Z. Fu, Y. Lu, *J. Mater. Chem. A* **2020**, *8*, 13150–13159.
- [41] a) N. Zhang, Y. Chai, *Energy Environ. Sci.* **2021**, *14*, 4647–4671; b) A. Grimaud, W. T. Hong, Y. Shao-Horn, J. M. Tarascon, *Nat. Mater.* **2016**, *15*, 121–126.
- [42] a) A. Grimaud, O. Diaz-Morales, B. Han, W. T. Hong, Y.-L. Lee, L. Giordano, K. A. Stoerzinger, M. T. M. Koper, Y. Shao-Horn, *Nat. Chem.* **2017**, *9*, 457–465; b) S. Lee, K. Banjac, M. Lingenfelder, X. Hu, *Angew. Chem. Int. Ed.* **2019**, *58*, 10295–10299; *Angew. Chem.* **2019**, *131*, 10401–10405; c) C. Roy, B. Sebok, S. B. Scott, E. M. Fiordaliso, J. E. Sørensen, A. Bodin, D. B. Trimarco, C. D. Damsgaard, P. C. K. Vesborg, O. Hansen, I. E. L. Stephens, J. Kibsgaard, I. Chorkendorff, *Nat. Catal.* **2018**, *1*, 820–829.
- [43] a) X. Ren, C. Wei, Y. Sun, X. Liu, F. Meng, X. Meng, S. Sun, S. Xi, Y. Du, Z. Bi, G. Shang, A. C. Fisher, L. Gu, Z. J. Xu, *Adv. Mater.* **2020**, *32*, 2001292; b) J. Wu, Z. Zhuo, X. Rong, K. Dai, Z. Lebens-Higgins, S. Sallis, F. Pan, L. F. J. Piper, G. Liu, Y.-d. Chuang, Z. Hussain, Q. Li, R. Zeng, Z.-x. Shen, W. Yang, *Sci. Adv.* **2020**, *6*, eaaw3871.
- [44] a) L. C. Seitz, C. F. Dickens, K. Nishio, Y. Hikita, J. Montoya, A. Doyle, C. Kirk, A. Vojvodic, H. Y. Hwang, J. K. Nørskov, T. F. Jaramillo, *Science*

- 2016, 353, 1011–1014; b) I. C. Man, H.-Y. Su, F. Calle-Vallejo, H. A. Hansen, J. I. Martínez, N. G. Inoglu, J. Kitchin, T. F. Jaramillo, J. K. Nørskov, J. Rossmeisl, *ChemCatChem* **2011**, *3*, 1159–1165.
- [45] a) M. Wohlfahrt-Mehrens, J. Heitbaum, *J. Electroanal. Chem. Interfacial Electrochem.* **1987**, *237*, 251–260; b) Y. Tian, S. Wang, E. Velasco, Y. Yang, L. Cao, L. Zhang, X. Li, Y. Lin, Q. Zhang, L. Chen, *iScience* **2020**, *23*, 100756.
- [46] a) S. Cherevko, T. Reier, A. R. Zeradjanin, Z. Pawolek, P. Strasser, K. J. J. Mayrhofer, *Electrochem. Commun.* **2014**, *48*, 81–85; b) H. N. Nong, T. Reier, H.-S. Oh, M. Gliech, P. Paciok, T. H. T. Vu, D. Teschner, M. Heggen, V. Petkov, R. Schlögl, T. Jones, P. Strasser, *Nat. Catal.* **2018**, *1*, 841–851.
- [47] Z.-F. Huang, J. Song, Y. Du, S. Xi, S. Dou, J. M. V. Nsanzimana, C. Wang, Z. J. Xu, X. Wang, *Nat. Energy* **2019**, *4*, 329–338.
- [48] D. B. Hibbert, C. R. Churchill, *J. Chem. Soc. Faraday Trans.* **1984**, *80*, 1965–1975.
- [49] a) J. R. Petrie, H. Jeen, S. C. Barron, T. L. Meyer, H. N. Lee, *J. Am. Chem. Soc.* **2016**, *138*, 7252–7255; b) E. M. Miner, M. Dincă, *Nat. Energy* **2016**, *1*, 16186.
- [50] a) S. S. Shinde, C. H. Lee, J.-Y. Jung, N. K. Wagh, S.-H. Kim, D.-H. Kim, C. Lin, S. U. Lee, J.-H. Lee, *Energy Environ. Sci.* **2019**, *12*, 727–738; b) J. Lee, O. K. Farha, J. Roberts, K. A. Scheidt, S. T. Nguyen, J. T. Hupp, *Chem. Soc. Rev.* **2009**, *38*, 1450–1459.
- [51] a) C. Qu, B. Zhao, Y. Jiao, D. Chen, S. Dai, B. M. deGlee, Y. Chen, K. S. Walton, R. Zou, M. Liu, *ACS Energy Lett.* **2017**, *2*, 1263–1269; b) Z. Xiao, Y. Mei, S. Yuan, H. Mei, B. Xu, Y. Bao, L. Fan, W. Kang, F. Dai, R. Wang, L. Wang, S. Hu, D. Sun, H.-C. Zhou, *ACS Nano* **2019**, *13*, 7024–7030.
- [52] H. Zhang, B. Xu, H. Mei, Y. Mei, S. Zhang, Z. Yang, Z. Xiao, W. Kang, D. Sun, *Small* **2019**, *15*, 1904663.
- [53] X. Liu, F. Xia, R. Guo, M. Huang, J. Meng, J. Wu, L. Mai, *Adv. Funct. Mater.* **2021**, *31*, 2101792.
- [54] J. Zhou, Y. Dou, X.-Q. Wu, A. Zhou, L. Shu, J.-R. Li, *Small* **2020**, *16*, 1906564.
- [55] M. Liu, L. Kong, X. Wang, J. He, X.-H. Bu, *Small* **2019**, *15*, 1903410.
- [56] W. Zheng, M. Liu, L. Y. S. Lee, *ACS Catal.* **2020**, *10*, 81–92.
- [57] S. Hou, W. Li, S. Watzele, R. M. Kluge, S. Xue, S. Yin, X. Jiang, M. Döblinger, A. Welle, B. Garlyyev, M. Koch, P. Müller-Buschbaum, C. Wöll, A. S. Bandarenka, R. A. Fischer, *Adv. Mater.* **2021**, *33*, 2103218.
- [58] M. Liu, L. Kong, X. Wang, J. He, J. Zhang, J. Zhu, X.-H. Bu, *Nano Res.* **2021**.
- [59] A. I. Khan, D. O'Hare, *J. Mater. Chem.* **2002**, *12*, 3191–3198.
- [60] a) S. Zhao, C. Tan, C.-T. He, P. An, F. Xie, S. Jiang, Y. Zhu, K.-H. Wu, B. Zhang, H. Li, J. Zhang, Y. Chen, S. Liu, J. Dong, Z. Tang, *Nat. Energy* **2020**, *5*, 881–890; b) K. S. Park, Z. Ni, A. P. Côté, J. Y. Choi, R. Huang, F. J. Uribe-Romo, H. K. Chae, M. O'Keeffe, O. M. Yaghi, *Proc. Natl. Acad. Sci. USA* **2006**, *103*, 10186–10191.
- [61] T. Liu, P. Li, N. Yao, T. Kong, G. Cheng, S. Chen, W. Luo, *Adv. Mater.* **2019**, *31*, 1806672.
- [62] B. Zhang, Z. Qi, Z. Wu, Y. H. Lui, T.-H. Kim, X. Tang, L. Zhou, W. Huang, S. Hu, *ACS Energy Lett.* **2019**, *4*, 328–336.
- [63] W. Li, S. Watzele, H. A. El-Sayed, Y. Liang, G. Kieslich, A. S. Bandarenka, K. Rodewald, B. Rieger, R. A. Fischer, *J. Am. Chem. Soc.* **2019**, *141*, 5926–5933.
- [64] J. C. Mankins, *Acta Astronaut.* **2009**, *65*, 1216–1223.
- [65] Z. Chen, M. C. Wasson, R. J. Drout, L. Robison, K. B. Idrees, J. G. Knapp, F. A. Son, X. Zhang, W. Hierse, C. Kühn, S. Marx, B. Hernandez, O. K. Farha, *Faraday Discuss.* **2021**, *225*, 9–69.
- [66] a) P. He, Y. Xie, Y. Dou, J. Zhou, A. Zhou, X. Wei, J.-R. Li, *ACS Appl. Mater. Interfaces* **2019**, *11*, 41595–41601; b) K. Wan, J. Luo, C. Zhou, T. Zhang, J. Arbiol, X. Lu, B.-W. Mao, X. Zhang, J. Fransaer, *Adv. Funct. Mater.* **2019**, *29*, 1900315; c) Z. Wan, D. Yang, J. Chen, J. Tian, T. T. Isimjan, X. Yang, *ACS Appl. Nano Mater.* **2019**, *2*, 6334–6342; d) L. Yu, J. F. Yang, B. Y. Guan, Y. Lu, X. W. Lou, *Angew. Chem. Int. Ed.* **2018**, *57*, 172–176; *Angew. Chem.* **2018**, *130*, 178–182; e) Y. Xu, S. Hou, G. Yang, X. Wang, T. Lu, L. Pan, *Electrochim. Acta* **2018**, *285*, 192–201.
- [67] a) Y. Zhang, J. Fu, H. Zhao, R. Jiang, F. Tian, R. Zhang, *Appl. Catal. B* **2019**, *257*, 117899; b) W. He, R. Ifraemov, A. Raslin, I. Hod, *Adv. Funct. Mater.* **2018**, *28*, 1707244.
- [68] A. P. Murthy, J. Theerthagiri, J. Madhavan, *J. Phys. Chem. C* **2018**, *122*, 23943–23949.
- [69] M. R. Gennero de Chialvo, A. C. Chialvo, *Electrochim. Acta* **1998**, *44*, 841–851.
- [70] a) W. Sheng, Z. Zhuang, M. Gao, J. Zheng, J. G. Chen, Y. Yan, *Nat. Commun.* **2015**, *6*, 5848; b) T. J. Schmidt, P. N. Ross, N. M. Markovic, *J. Electroanal. Chem.* **2002**, *524–525*, 252–260; c) S. Watzele, J. Fichtner, B. Garlyyev, J. N. Schwämmlein, A. S. Bandarenka, *ACS Catal.* **2018**, *8*, 9456–9462.
- [71] E. Skúlason, V. Tripkovic, M. E. Björketun, S. Gudmundsdóttir, G. Karlberg, J. Rossmeisl, T. Bligaard, H. Jónsson, J. K. Nørskov, *J. Phys. Chem. C* **2010**, *114*, 18182–18197.
- [72] a) R. Subbaraman, D. Tripkovic, D. Strmcnik, K.-C. Chang, M. Uchimura, A. P. Paulikas, V. Stamenkovic, N. M. Markovic, *Science* **2011**, *334*, 1256–1260; b) R. Subbaraman, D. Tripkovic, K.-C. Chang, D. Strmcnik, A. P. Paulikas, P. Hirunsit, M. Chan, J. Greeley, V. Stamenkovic, N. M. Markovic, *Nat. Mater.* **2012**, *11*, 550–557; c) S. Xue, R. W. Haid, R. M. Kluge, X. Ding, B. Garlyyev, J. Fichtner, S. Watzele, S. Hou, A. S. Bandarenka, *Angew. Chem. Int. Ed.* **2020**, *59*, 10934–10938; *Angew. Chem.* **2020**, *132*, 11026–11031.
- [73] Y. Xu, S. Yu, T. Ren, S. Liu, Z. Wang, X. Li, L. Wang, H. Wang, *ACS Appl. Mater. Interfaces* **2020**, *12*, 34728–34735.
- [74] P. Horcajada, S. Surblé, C. Serre, D.-Y. Hong, Y.-K. Seo, J.-S. Chang, J.-M. Grenèche, I. Margiolaki, G. Férey, *Chem. Commun.* **2007**, 2820–2822.
- [75] R. Nivetha, K. Gothandapani, V. Raghavan, G. Jacob, R. Sellappan, P. Bhardwaj, S. Pitchaimuthu, A. N. M. Kannan, S. K. Jeong, A. N. Grace, *ACS Omega* **2020**, *5*, 18941–18949.
- [76] S. Jabarian, A. Ghaffarinejad, *J. Inorg. Organomet. Polym. Mater.* **2019**, *29*, 1565–1574.
- [77] a) Y.-H. Chang, W. Zhang, Y. Zhu, Y. Han, J. Pu, J.-K. Chang, W.-T. Hsu, J.-K. Huang, C.-L. Hsu, M.-H. Chiu, T. Takenobu, H. Li, C.-I. Wu, W.-H. Chang, A. T. S. Wee, L.-J. Li, *ACS Nano* **2014**, *8*, 8582–8590; b) D. Kang, T. W. Kim, S. R. Kubota, A. C. Cardiel, H. G. Cha, K.-S. Choi, *Chem. Rev.* **2015**, *115*, 12839–12887.
- [78] T. Lochner, R. M. Kluge, J. Fichtner, H. A. El-Sayed, B. Garlyyev, A. S. Bandarenka, *ChemElectroChem* **2020**, *7*, 3545–3568.
- [79] B. Garlyyev, S. Watzele, J. Fichtner, J. Michalička, A. Schökel, A. Senyshyn, A. Perego, D. Pan, H. A. El-Sayed, J. M. Macak, P. Atanassov, I. V. Zenyuk, A. S. Bandarenka, *Nano Res.* **2021**, *14*, 2762–2769.
- [80] a) H. Wang, B.-H. Chen, D.-J. Liu, *Adv. Mater.* **2021**, *33*, 2008023; b) S. Gonen, L. Elbaz, *Curr. Opin. Electrochem.* **2018**, *9*, 179–188.
- [81] a) B. Garlyyev, Y. Liang, S. Xue, S. Watzele, J. Fichtner, W.-J. Li, X. Ding, A. S. Bandarenka, *Curr. Opin. Electrochem.* **2019**, *14*, 206–213; b) B. Garlyyev, J. Fichtner, O. Piqué, O. Schneider, A. S. Bandarenka, F. Calle-Vallejo, *Chem. Sci.* **2019**, *10*, 8060–8075.
- [82] E. M. Miner, S. Gul, N. D. Ricke, E. Pastor, J. Yano, V. K. Yachandra, T. Van Voorhis, M. Dincă, *ACS Catal.* **2017**, *7*, 7726–7731.
- [83] X.-H. Liu, W.-L. Hu, W.-J. Jiang, Y.-W. Yang, S. Niu, B. Sun, J. Wu, J.-S. Hu, *ACS Appl. Mater. Interfaces* **2017**, *9*, 28473–28477.
- [84] K. Cho, S.-H. Han, M. P. Suh, *Angew. Chem. Int. Ed.* **2016**, *55*, 15301–15305; *Angew. Chem.* **2016**, *128*, 15527–15531.
- [85] K. Kratzl, T. Kratzky, S. Günther, O. Tomanec, R. Zbořil, J. Michalička, J. M. Macak, M. Cokoja, R. A. Fischer, *J. Am. Chem. Soc.* **2019**, *141*, 13962–13969.
- [86] a) G.-L. Chai, K. Qiu, M. Qiao, M.-M. Titirici, C. Shang, Z. Guo, *Energy Environ. Sci.* **2017**, *10*, 1186–1195; b) G. Rothenberg, **2008**, *Catalysts: concepts and green applications*, Wiley-VCH, Weinheim, p. 65.
- [87] W. Li, S. Xue, S. Watzele, S. Hou, J. Fichtner, A. L. Semrau, L. Zhou, A. Welle, A. S. Bandarenka, R. A. Fischer, *Angew. Chem. Int. Ed.* **2020**, *59*, 5837–5843; *Angew. Chem.* **2020**, *132*, 5886–5892.
- [88] F. N. Al-Rowaili, A. Jamal, M. S. Ba Shammakh, A. Rana, *ACS Sustainable Chem. Eng.* **2018**, *6*, 15895–15914.
- [89] J.-D. Yi, R. Xie, Z.-L. Xie, G.-L. Chai, T.-F. Liu, R.-P. Chen, Y.-B. Huang, R. Cao, *Angew. Chem. Int. Ed.* **2020**, *59*, 23641–23648; *Angew. Chem.* **2020**, *132*, 23849–23856.
- [90] W.-W. Yuan, J.-X. Wu, X.-D. Zhang, S.-Z. Hou, M. Xu, Z.-Y. Gu, *J. Mater. Chem. A* **2020**, *8*, 24486–24492.
- [91] R. Kortlever, J. Shen, K. J. P. Schouten, F. Calle-Vallejo, M. T. M. Koper, *J. Phys. Chem. Lett.* **2015**, *6*, 4073–4082.
- [92] Z. W. Seh, J. Kibsgaard, C. F. Dickens, I. Chorkendorff, J. K. Nørskov, T. F. Jaramillo, *Science* **2017**, *355*, eaad4998.
- [93] J. Liu, S. Hou, W. Li, A. S. Bandarenka, R. A. Fischer, *Chem. Asian J.* **2019**, *14*, 3474–3501.
- [94] M.-D. Zhang, D.-H. Si, J.-D. Yi, Q. Yin, Y.-B. Huang, R. Cao, *Sci. China Chem.* **2021**, *64*, 1332–1339.
- [95] P. Lamagni, M. Miola, J. Catalano, M. S. Hvid, M. A. H. Mamakhel, M. Christensen, M. R. Madsen, H. S. Jeppesen, X.-M. Hu, K. Daasbjerg, T. Skrydstrup, N. Lock, *Adv. Funct. Mater.* **2020**, *30*, 1910408.
- [96] B. Zhang, S. Cao, Y. Wu, P. Zhai, Z. Li, Y. Zhang, Z. Fan, C. Wang, X. Zhang, J. Hou, L. Sun, *ChemElectroChem* **2021**, *8*, 880–886.
- [97] N. Li, P. Yan, Y. Tang, J. Wang, X.-Y. Yu, H. B. Wu, *Appl. Catal. B* **2021**, *297*, 120481.

- [98] <https://www.ccdc.cam.ac.uk/Community/csd-community/csd-mof-collection/>, Cambridge Crystallographic Data Centre, accessed on 23-10-2021.
- [99] Y. Xu, Q. Li, H. Xue, H. Pang, *Coord. Chem. Rev.* **2018**, *376*, 292–318.
- [100] a) S. Tajik, H. Beitollahi, F. G. Nejad, K. O. Kirlikovali, Q. Van Le, H. W. Jang, R. S. Varma, O. K. Farha, M. Shokouhimehr, *Cryst. Growth Des.* **2020**, *20*, 7034–7064; b) R. Du, Y. Wu, Y. Yang, T. Zhai, T. Zhou, Q. Shang, L. Zhu, C. Shang, Z. Guo, *Adv. Energy Mater.* **2021**, *11*, 2100154.
- [101] a) M. Zhong, K. Tran, Y. Min, C. Wang, Z. Wang, C.-T. Dinh, P. De Luna, Z. Yu, A. S. Rasouli, P. Brodersen, S. Sun, O. Voznyy, C.-S. Tan, M. Askerka, F. Che, M. Liu, A. Seifitokaldani, Y. Pang, S.-C. Lo, A. Ip, Z. Ulissi, E. H. Sargent, *Nature* **2020**, *581*, 178–183; b) R. Ding, Y. Chen, P. Chen, R. Wang, J. Wang, Y. Ding, W. Yin, Y. Liu, J. Li, J. Liu, *ACS Catal.* **2021**, *11*, 9798–9808.
- [102] N. Zhang, B. Yang, K. Liu, H. Li, G. Chen, X. Qiu, W. Li, J. Hu, J. Fu, Y. Jiang, M. Liu, J. Ye, *Small Methods*, *n/a*, 2100987.
- [103] M. Ding, X. Cai, H.-L. Jiang, *Chem. Sci.* **2019**, *10*, 10209–10230.

Manuscript received: October 30, 2021
Revised manuscript received: December 12, 2021
Accepted manuscript online: December 14, 2021